Analysis of surface wind and roughness length evolution with fetch using a combination of airborne lidar and radar measurements

Cyrille Flamant, Jacques Pelon, Danièle Hauser, Céline Quentin, William M. Drennan, Francis Gohin, Bertrand Chapron, Jrome Gourrion

JOURNAL OF GEOPHYSICAL RESEARCH, VOL. 108, NO. C3, 8058, doi:10.1029/2002JC001405, 2003

Analysis of surface wind and roughness length evolution with fetch using a combination of airborne lidar and radar measurements

Cyrille Flamant and Jacques Pelon
Service d'Aéronomie/IPSL, Université Pierre et Marie Curie, Paris, France

Daniéle Hauser and Céline Quentin
Centre d'Étude des Environnements Planétaires/IPSL, Université St Quentin-Versailles, Vélizy, France

William M. Drennan
Rosenstiel School of Marine and Atmospheric Science, University of Miami, Miami, Florida, USA

Francis Gohin, Bertrand Chapron, and Jrome Gourrion
Département d'Océanographie Spatiale, Institut Français de Recherche pour l'Exploitation de la Mer, Brest, France

Received 25 March 2001; revised 19 July 2002; accepted 20 July 2002; published 13 February 2003.

[1] A combination of surface wind speed (SWS) and sea state variables, derived from quasi-simultaneous airborne lidar and radar measurements, made in the framework of the Flux, État de mer et Télédétection en Condition de fetcH variable (FETCH) experiment, is used to analyze the evolution of surface roughness length, neutral drag coefficient, and friction velocity coefficient with fetch in the first hundred kilometers offshore over the Gulf of Lion, Western Mediterranean. The study focuses on the Tramontane/Mistral event documented in the afternoon of 24 March 1998. Particular attention is given to SWS derived from nadir lidar measurements. The SWS retrieval methodology developed and validated for open ocean conditions by *Flamant et al.* [1998] has been modified to account for the specificity of the coastal Mediterranean environment (complex mixture of continental and maritime aerosol; turbid, productive waters). The lidar-derived SWS evolution with fetch observed on 24 March 1998 in the afternoon was validated against in situ and remote sensing measurements made from a buoy, a ship, as well as from the spaceborne altimeter TOPEX. The spatial variability in SWS observed with the airborne lidar was controlled by the structure of the wake regions downstream of the Massif Central and the Maritime Alps, delimiting the longitudinal extension of the Mistral, and was influenced by swell resulting from the action of a steady northeasterly flow coming from the Ligurian Sea in connection with intense Alpine lee cyclogenesis. These findings were supported by the other measurements. It is further shown that, based on a formulation of the dimensionless roughness dependance with wave age, airborne lidar and radar measurements can be combined to provide insight into the evolution with fetch of roughness length, neutral drag coefficient, and friction velocity. Four distinct sea state regimes over a distance of 100 km could be identified from the remotely sensed variables obtained with this novel approach in connection with atmospheric forcing. The dependance of lidar/radar derived drag coefficient with lidar-derived SWS for the four regimes was found to be remarkably consistent with the relationship derived from the buoy measurements. Finally, lidar/radar derived friction velocities were found in good agreement with the buoy and in situ aircraft measurements. *INDEX TERMS:* 3339 Meteorology and Atmospheric Dynamics: Ocean/atmosphere interactions (0312, 4504); 3360 Meteorology and Atmospheric Dynamics: Remote sensing; 4506 Oceanography: Physical: Capillary waves

Citation: Flamant, C., J. Pelon, D. Hauser, C. Quentin, W. M. Drennan, F. Gohin, B. Chapron, and J. Gourrion, Analysis of surface wind and roughness length evolution with fetch using a combination of airborne lidar and radar measurements, *J. Geophys. Res.*, *108*(C3), 8058, doi:10.1029/2002JC001405, 2003.

0148-0227/03/2002JC001405

1. Introduction

[2] The air-sea flux of momentum in the marine atmospheric boundary layer (MABL) is a key boundary parameter for atmospheric, oceanic and wave models. It is

related to the "roughness" of the waves and depends on atmospheric wind speed, atmospheric stability, locally generated wind-waves (i.e., their size, shape and phase velocity) as well as swell [e.g., *Hwang and Shemdin*, 1988; *Vickers and Mahrt*, 1997 and references therein; *Drennan et al*., 2003].

[3] To this day, most of the process-oriented investigations dedicated to the analysis of momentum flux in limited fetch conditions have been conducted from still and slowly moving sea-borne platforms, i.e., buoys, ships, offshore towers or a combination of platforms (e.g., RASEX (Riso Air Sea EXperiment) [*Mahrt et al.*, 1996] or WAVES (Water-Air Vertical Exchange Study), SWADE (Surface Wave dynamics Experiment) and HEXOS (Humidity Exchange over the Sea), see a brief overview of these experiments in the work of *Drennan et al*. [2003]. In such studies, the variety of the fetch conditions encountered at the platform results essentially from the variety of wind conditions observed in the course of an experiment. Direct measurement of momentum fluxes in the MABL (by eddy-correlation or inertial dissipation techniques) require statistically representative sets of data (i.e., long integration times) and assume quasi-stationary conditions at the point of measurements.

[4] In contrast, the study of momentum transfer evolution with fetch in offshore conditions has been a largely neglected area of research, until now, due to the fact that momentum flux are difficult to measure from airborne platforms. Concerning these fluxes, representativity and uncertainty issues arise from: (1) the difficulty of making measurements in the shallow surface layer (i.e., the "constant flux" layer) with an aircraft and (2) the technique employed to measure the fluxes (i.e., an eddy correlation technique). The eddy correlation technique requires thermodynamical variables to be accumulated over a statistically representative sample (i.e., 20–25 km) in which case the assumption of quasi-stationary conditions is not valid. Moreover, the horizontal resolution of such measurements (20–25 km) far exceeds the resolution need to examine surface related processes.

[5] The study of momentum flux evolution with fetch, in the "Lagrangian" sense, is highly desirable for a better comprehension of momentum transfer at the mesoscale and improving coupled ocean-atmosphere circulation models in coastal regions. Remote sensing of surface variables from airborne platforms appears to be the natural link between local measurements from buoys and ships and those retrieved at the mesoscale from spaceborne platforms and simulated by atmospheric models. The parameterization of surface flux from remotely sensed variables needs to be developed.

[6] In this paper, we propose a novel approach combining airborne radar and lidar measurements to determine, in a coastal region, the evolution with fetch of variables which are key to the understanding and parameterization of momentum fluxes, i.e., roughness length and drag coefficient.

[7] The capability of airborne radar ocean wave spectrometers to provide precise, high spatial resolution measurements of surface wind speed, significant wave height and wave peak frequency has been demonstrated repeatedly [*Jackson et al.*, 1985; *Hauser et al.*, 1992, 1995; *Banner et al.*, 1999; *Pettersson et al.*, 2003]. More recently, airborne lidars have shown promising potential for providing accurate highly resolved surface wind speed (SWS) over the ocean [e.g., *Bufton et al.*, 1983; *Flamant et al.*, 1998]. As discussed by these authors, sea surface reflectance can be inferred from airborne nadir lidar measurements by analyzing the interaction of the laser pulse with the sea surface. Provided that atmospheric effects (variability in both aerosol composition, aerosol concentration and relative humidity) and oceanic effects (the contribution of the submarine reflectance) can be corrected for, the sea surface reflectance can be related to the surface mean square slope produced by capillary and gravity waves riding on longer waves. Surface mean square slope can then be interpreted in terms of SWS using the comprehensive work of *Cox and Munk* [1954]. This technique has also been applied successfully to spaceborne lidar data acquire during the Lidar In-space Technology Experiment [*Menzies et al.*, 1998].

[8] In this paper, we use a combination of airborne lidar and radar measurements acquired in the framework of the Flux, État de mer et Télédétection en Condition de fetcH variable (FETCH) experiment [*Hauser et al.*, 2003, 2002], to analyze the evolution of sea state variables with fetch in the first hundred kilometers offshore over the Gulf of Lion (GoL), Western Mediterranean. The study focuses on the Tramontane/Mistral event documented in the afternoon of 24 March 1998. The Tramontane and the Mistral are low level, orography-induced, cold-air outbreaks over the GoL blowing offshore of Narbonne and Arles, France, respectively (Figure 1). They are frequently observed to extend several hundreds of kilometers from the coast, bringing cold and dry continental air over the warm Western Mediterranean, and hence, generating intense heat air-sea exchanges. They are one of the primary cause of storms over the Mediterranean, between Italy and the Balearic Islands [*Trigo et al.*, 1999; *Campins et al.*, 2000].

[9] The analysis also relies on the measurements at sea performed by a moored buoy and a ship specially deployed for the experiment, as well as measurements from the TOPEX altimeter. This paper addresses several questions, including the following:

1. Can SWS be inferred from lidar measurements over the sea in a coastal environment (complex mixture of continental and maritime aerosol; turbid, productive waters)?
2. What is the influence of developing waves on the lidar-derived surface mean square slope and related SWS?
3. How does spatial evolution of sea state variables (SWS, roughness length and drag coefficient) with fetch derived from airborne measurements compare with the temporal evolution of these variables derived from a moored buoy?

[10] In section 2, we present the synoptic situation and the FETCH operations on 24 March 1998. In section 3, we describe the methodology used to derive sea state variables from lidar (SWS) and a combination of lidar and radar data (roughness length and drag coefficient) over coastal waters. In section 4, we discuss the evolution of surface mean square slope measured by airborne lidar, airborne radar (C-Band) and spaceborne radar (C-Band and Ku-Band). We compare the evolution of lidar-derived SWS and roughness

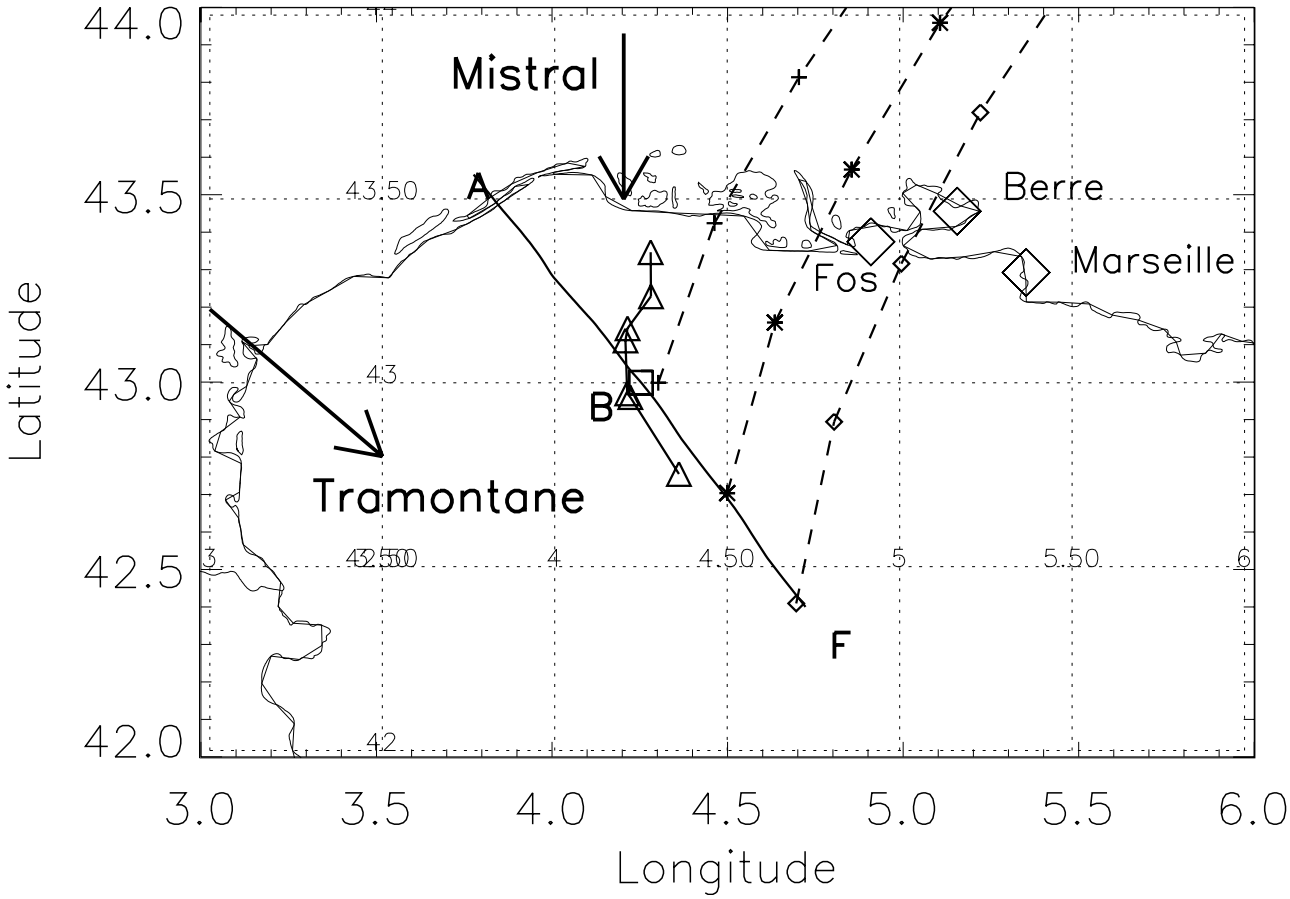

Figure 1. Leg AF of the ARAT flight track between 1620 and 1640 UTC on 24 March 1998. The location of the cities of Fos, Berre and Marseille are indicated. Superimposed are the isentropic backtrajectories (dashed lines) ending in different part of leg AF on 24 March 1998 at 1600 UTC. The trajectories describe the aerosol transport at about 500 m ASL. The rugged solid line represents the coastline. The position of the Research Vessel Atalante at (from south to north): 0900, 1245, 1345, 1545, 1600, 1700, 2050 and 2210 UTC are indicated by triangles. The position of the ASIS buoy is indicated by the square symbol. The thick arrows indicate the climatologically representative directions of the Mistral and Tramontane winds.

length with measurements made from other platforms (i.e., sea-borne, ship-borne, airborne and spaceborne platforms). We also discuss the spatial evolution of the momentum flux drag coefficient derived from airborne measurements. Concluding remarks are in section 5.

2. The 24 March 1998 Case of Fetch: Synoptic Situation and Operations

[11] In addition to the means specially deployed for FETCH, Météo-France provided daily forecasts of the meteorological situation made with the operational model ALADIN. The forecasts on 24 March 1998 have been validated against buoy, ship and aircraft in situ data [*Flamant*, 2003]. These comparisons confirmed that the thermodynamical conditions prevailing over the GoL during the afternoon airborne operations (see below) were well represented by the 1800 UTC ALADIN forecast. In turn, the ALADIN forecasts were used by *Flamant* [2003] to analyze the rapid evolution of the synoptic situation on 24 March 1998. As these forecasts are also utilized in this study, we first briefly present the ALADIN model.

[12] ALADIN is a spectral limited area model, taking its boundary conditions from the global model ARPEGE of Météo-France, which covers a domain of 2739 km × 2739 km (centered on France). The horizontal resolution is approximately 10 km, with 31 levels on the vertical, the highest level being at 5 hPa and the lowest level at approximately 17 m above ground/sea level. The surface layer and planetary boundary layer fluxes are computed on the lowest level using a modified version of the scheme developed by *Louis et al.* [1981]. The 3D-var data assimilation provides two analyses per day (0000 and 1200 UTC) but no associated first guess. Forecasts are available every 3-h, i.e., at 0000, 0300, 0600, 0900, 1200, 1500, 1800, 2100 and 2400 UTC. 3-h integrated surface turbulent fluxes are computed from 12-h forecasts. Additional information can be found in the work of *Eymard et al.* [2003]. The forecasts products are: temperature, humidity and wind distributed on 16 pressure levels between 1000 and 100 hPa. Sea level pressure and surface turbulent fluxes are provided at the lowest level, i.e., 17 m ASL. Near surface extrapolated fields (at 10 m ASL for the wind and 2 m ASL for temperature and humidity) are derived assuming a neutral

profile. The SST in the model is issued from Reynolds' climatology and yields characteristic spatial and temporal scales of about 2° and 8 days, respectively.

2.1. Synoptic Situation

[13] Based on ALADIN forecasts, *Flamant* [2003] has shown that the nonstationary nature of the Tramontane/Mistral wind regime over the GoL on 24 March 1998 was controlled by the multistage evolution of an Alpine lee cyclone over the Tyrrhenian Sea (between Sardinia and continental Italy). In the early stage, the Tramontane flow prevailed over the GoL. As the low deepened, the prevailing wind regime shifted to a well established Mistral which peaked around 1200 UTC. In the afternoon, the Mistral was progressively disrupted by a strengthening outflow coming from the Ligurian Sea in response to the deepening low over the Tyrrhenian Sea and the channeling induced by the presence of the Apennine range (Italy) and the Alps. In the evening, the Mistral was again well established over the GoL as the depression continued to deepen but moved to the south-east, reducing the influence of outflow from the Ligurian Sea on the flow over the GoL.

2.2. Operations

[14] On 24 March 1998, measurements of the mean and turbulent properties within the ABL over the GoL were made from four platforms: two aircraft (the ARAT—Avion de Recherche Atmosphérique et Télédétection—and the Merlin IV), the Research Vessel Atalante and the Air-Sea Interaction Spar (ASIS) buoy. The operations were coordinated with TOPEX descending overpass 146 (1844 UTC).

[15] The Research Vessel Atalante had balloon launching capability and carried an instrumented mast for mean and turbulent measurements at a height of 17 m above the sea surface. The ASIS buoy [*Graber et al.*, 2000] made measurements of mean and turbulent atmospheric variables 7 m above the air-sea interface as well as wave directional spectra. The ARAT and Merlin IV were equipped with standard in situ sensors as well as sensors dedicated to the analysis of aerosol properties (nephelometer, particle and cloud condensation nuclei counters). The ARAT and the Merlin IV also embarked the differential absorption lidar LEANDRE 2 [*Bruneau et al.*, 2001a, 2001b] and the real-aperture airborne radar RESSAC (Radar pour l'Etude du Spectre de Surface par Analyze Circulaire) [*Hauser et al.*, 1992], respectively. RESSAC is a C-Band radar, with a large antenna (14° elevation × 3.4° azimuth) looking at a mean incidence angle of 12° from a flight altitude of about 6 km ASL. The processing of the wave measurements is done following *Hauser et al.* [1992], and is based on the measurement of the modulation of the radar backscatter coefficient due to slopes of the longer waves (wavelength between 40 to 400 m).

[16] In the afternoon of 24 March 1998, the ARAT flew an X-shaped pattern at 3.9 km above sea level (ASL) from 1620 to 1730 UTC, with LEANDRE 2 looking to the surface. The lidar measurements of interest for this study were acquired along leg AF (Figure 1) between 1620 and 1640 UTC. The flight was coordinated with a TOPEX overpass and designed such that leg AF coincide with the satellite ground track. The ARAT also performed a sounding in the vicinity of waypoint F. Between 1741 and 1828 UTC, the Merlin IV flew along leg AF at 6 km ASL with RESSAC functioning in the so-called wave mode and providing directional wave spectra. Directional wave spectra measured by RESSAC were normalized using the significant wave height measured by TOPEX altimeter along the same track and less than one hour after. Overflights of ASIS by the Merlin and the ARAT occurred at 1746 UTC and 1632 UTC, respectively.

[17] The position of ASIS buoy is indicated by the square symbol in Figure 1. The position of the Research Vessel Atalante between 0900 and 2200 UTC is indicated by triangles in Figure 1.

[18] Water vapor and atmospheric reflectivity (732 nm) fields monitored with the downward-pointing LEANDRE 2 during this flight have been analyzed by *Flamant et al.* [2003] and *Flamant* [2003], respectively. The diameter of the laser footprint at the surface for a single laser pulse is less than 9 m. In the following, sea surface reflectances are obtained from 20 averaged lidar profiles. Sea state variables estimated with RESSAC were obtained by averaging over five antenna rotations (100 s). The footprint at the surface is 0.4 km × 1.5 km for an aircraft flying at 6 km ASL.

3. Methodology for Sea State Variable Retrieval

[19] At this point, it should be noted that the airborne lidar LEANDRE 2 was not developed for the primary purpose of measuring SWS [LEANDRE 2 was developed for the purpose of analyzing surface-atmosphere exchanges through the ABL]. This implies careful lidar calibration and inversion as described in Appendices A and B. A lidar system specifically developed for the purpose of measuring SWS [e.g., a system with longer wavelength and multiple look angles] would alleviate some of the limitations of the calibration and inversion approach described in this paper.

[20] To analyze the lidar data acquired during FETCH, the SWS retrieval methodology developed and validated for open ocean conditions by *Flamant et al.* [1998] has been modified to account for the specificity of the coastal Mediterranean environment, namely: (1) coastal aerosol composition (to correct for atmospheric effects), (2) foam at the sea surface and air bubbles within the water and (3) submarine reflectance enhancement at 732 nm caused by the presence of Chlorophyll, inorganic suspended particles from terrestrial origin, yellow substances (in the Rhone river plume) or even mineral dust (deposited at the surface during Saharan dust outbreaks). Note that the foam and subsurface water contributions to the lidar signal can be separated in two distinct components: (1) one related to the solar radiation diffused by the subsurface waters and/or foam in the direction of the lidar telescope and (2) one related to the interactions between the laser pulse and the subsurface water and/or foam within the laser footprint. It is argued that solar radiation diffused by the subsurface waters (including that of suspended particulate) and/or foam in the direction of the lidar telescope is removed through "background" light correction applied to the lidar data (see Appendix A). Solar-stimulated Chlorophyll fluorescence is also argued not to be a factor at 732 nm.

[21] Atmospheric effects (variability in both aerosol composition, aerosol concentration and relative humidity) and their influence of sea surface reflectance (SSR) retrievals

from lidar are presented and discussed in Appendix B. Based on sensitivity analyses, it is shown that the composition of the coastal aerosol has little influence on lidar-derived SWS retrievals, but that the reference scattering coefficient (needed to retrieve the aerosol backscatter coefficient near the sea surface from the "lidar inversion" procedure, see Appendix B for details) must be known accurately.

[22] The next step is to separate the contribution of waves from those of submarine reflectance at 732 nm and whitecaps when analyzing the laser emitted photons backscattered toward the lidar telescope, in order to obtain the lidar-derived surface MSS. This is discussed below (section 3.1). The methodology for radar-derived surface MSS (from TOPEX and RESSAC) is presented in Appendix C. Lidar-derived SWS retrieval technique is discussed in section 3.2. Finally, the methodology combining radar-lidar measurements for the retrieval of roughness length and drag coefficient in presented in section 3.3. Some of the equations presented in the following depend explicitly on atmospheric stability conditions. For the sake of clarity, we have chosen to discuss the stability issue in this section rather than discussing it with the results in section 4. To do so, we have utilized ALADIN forecasts at 1800 UTC.

3.1. Lidar-Derived Surface Mean Square Slope

[23] Light reflection by the ocean surface has been observed to be dependent on the small wave facets that are produced by capillary and capillary-gravity waves at the surface superimposed upon the long-wave swell [e.g., *Cox and Munk*, 1954; *Bufton et al.*, 1983]. The light backscattered by whitecaps and the light backscattered from the first meters below the ocean surface also contributes to the measured surface reflectance. The total reflectance (which is the reflectance derived from lidar measurements) is written as [*Menzies et al.*, 1998]

$$\widehat{\rho} = W\rho_{f,eff} + (1 - W)\rho_s + (1 - W')\rho_{ssw}. \quad (1)$$

The first term is the reflectance associated with foam patches within the lidar solid angle of observation (i.e., footprint, ≈9 m), W being the area covered by whitecaps. $\rho_{f,eff}$ is the effective reflectance of whitecaps which can be considered as constant and equal to 22 ± 11% in the wind speed range of 4 to 25 m s^{-1} [*Koepke*, 1984]. The Fresnel reflectance, ρ_o, is taken equal to 0.02 at 0.73 μm [*Hale and Querry*, 1973]. The second term is the reflectance associated with the slope distribution of the capillary and capillary-gravity waves over the water surface that is not covered by foam. The third is the volumic reflectance of the subsurface water, with $W' = W\ \rho_{f,eff}$. For this term, the assumption is made that the reflectance of the foam patches is the same for incident light coming from above and below the surface [*Koepke*, 1984; *Menzies et al.*, 1998].

[24] An important parameter related to capillary and capillary-gravity waves and needed to interpret remote-sensing observations is their MSS. In the case of nadir lidar measurements (i.e., pitch and roll angles less than ±4° as was the case for the measurements considered here), the reflectance associated with capillary and capillary-gravity waves is given by

$$\rho_s = \frac{\rho_o}{4\langle S^2\rangle}, \quad (2)$$

where $\langle S^2\rangle$ is the total wave MSS variance. In this expression, the effects of laser pulse shape and divergence have been neglected as contributing very weakly owing to our measurement configuration [*Gardner et al.*, 1983]. The surface wave slope variance, $\langle S^2\rangle$, can then be linked to SWS through a linear relationship [*Cox and Munk*, 1954]. Provided that the contributions of whitecaps and subsurface can be corrected for, lidar measurements can be used to estimate SWSs.

[25] *Gordon and Morel* [1983] pointed out that the scattering from the water column that is penetrated by the light can be treated as a Lambertian reflector essentially at the surface. In clean ocean water (water molecules, organic and inorganic matter), this is generally less than 1% at 732 nm. In coastal regions, this term cannot necessarily be neglected in the near infra-red part of the spectrum due to the presence of suspended particulate (yellow matter, mineral dust or even anthropogenic aerosols such as soot). Furthermore, the production of air bubbles by breaking waves in the subsurface waters may lead to a contribution comparable to that of suspended solid particles [*Flatau et al.*, 2000]. Nevertheless, the volumic reflectance of the subsurface water due to the presence of particulates, bubbles and dissolved organic material is not a factor at 732 nm [see *Flatau et al.*, 2000, Figure 5] so that $\widehat{\rho}$ reduces to the sum of the first two terms in equation (1). Finally, the contribution from foam depends on the area covered with whitecaps. In the experiment design, the laser output energy was adjusted so that lidar surface returns were not saturated for small fractional whitecap coverage (low albedo). For a large fractional whitecap coverage, the high albedo associated with foam could induce a saturated surface return and a non linear response of the lidar system detector. The only efficient way to screen out this contribution is to discarded the lidar reflectivity profiles with saturated surface echoes. This is the case for the lidar data used in this paper. When the fractional area covered by whitecaps is small, the foam related reflectance needs to be assessed. It is argued that laser radiation backscattered by foam can be accounted for based on the work of *Koepke* [1984] and a power law relationship between whitecap coverage and SWS as discussed below.

3.2. Lidar-Derived Surface Wind Speed

[26] In section 3.1, we have shown that the surface MSS can be derived from lidar measurements. The next step is to link surface MSS to SWS. In an earlier work by *Cox and Munk* [1954], the surface MSS statistics have been observed to follow a near-Gaussian distribution in a two-dimensional plane, when wind direction effects are not considered. The wave MSS was found to depend on the SWS measured at 41 ft (12.4 m), according to

$$\langle S^2\rangle_{\mathrm{cm}} = 0.003 + 5.12\ 10^{-3}\ U_{41ft}. \quad (3)$$

[27] In the following, we have assumed that, to the first order, U_{41ft} was not very different from the wind speed at 10 m ASL (as discussed later, the difference was less than 0.4 m s^{-1}).

[28] Recent observations [e.g., *Hwang and Shemdin*, 1988; *Shaw and Churnside*, 2001] have indicated that atmospheric stability effects on the surface wave slope statistics must be considered in conditions for which the

Table 1. Mean and Turbulent Parameters Extracted From ALADIN 1800 UTC Forecast Along Leg AF[a]

Latitude, °N	Longitude, °E	U, m s^{-1}	T_w, °C	T_a, °C	R_i	u_*, m s^{-1}	L, m
43.5	3.8	9.3	13.8	12.2	−0.132	0.35	89
43.4	3.9	11.4	13.7	12.0	−0.092	0.43	172
43.3	4.0	12.3	13.6	11.8	−0.085	0.45	175
43.2	4.1	12.8	13.5	11.6	−0.080	0.47	181
43.1	4.2	13.0	13.4	11.7	−0.071	0.47	188
43.0	4.2	13.4	13.3	11.7	−0.067	0.47	181
42.9	4.3	13.4	13.4	11.8	−0.065	0.47	172
42.8	4.4	12.8	13.4	11.9	−0.067	0.46	164
42.7	4.5	11.8	13.5	12.1	−0.071	0.46	157
42.6	4.6	11.1	13.5	12.1	−0.076	0.45	155
42.5	4.6	10.0	13.5	12.2	−0.089	0.45	149
42.4	4.7	8.9	13.5	12.2	−0.114	0.45	143

[a]ΔT_a is the Air Temperature (°C), T_w is the Sea Temperature (°C), R_i is the Reduced Richardson Number, U is the Wind Speed Measured at 10 m ASL, u_* is the Friction Velocity and L is the Monin-Obukhov Length.

stability of the atmospheric surface layer departed from neutral stability (i.e., the observations of *Cox and Munk* [1954] were made in slightly positive stability conditions). *Shaw and Churnside* [2001] reported observations in the negative stability regime (air temperatures cooler than water temperatures), demonstrating increasing relative MSS (their MSS normalized by the Cox and Munk values) with increasing negative stability. The data discussed here was acquired in cold-air outbreak conditions for which the negative stability is expected be important. Accounting for atmospheric stability, the wave MSS is given by [*Shaw and Churnside*, 2001]

$$\langle S^2 \rangle = \left[0.003 + 5.12\ 10^{-3}\, U\right][1.42 - 2.8\, R_i], -0.23 < R_i < 0.27, \tag{4}$$

where R_i is the reduced Richardson number given by

$$R_i = (g \Delta T_{a-w} z)\left[T_w U^2\right]^{-1}, \tag{5}$$

with g the gravitational constant, ΔT_{a-w} the air-sea temperature difference (°C), T_w the sea temperature (°C) and U the wind speed measured at height z (10 m). Note that equation (3) and equation (4) are the same for $R_i = 0.15$ which corresponds approximately to the stability regime under which were acquired the wave MSS reported by *Cox and Munk* [1954]. The Richardson number along leg AF was estimated using ALADIN forecasts at 1800 UTC (see values of the above cited parameters in Table 1). It was estimated to range between −0.13 and −0.065, yielding a correction term for the wave MSS between 1.6 and 1.8 (i.e., for a given SWS, the wave MSS is a factor 1.7 ± 0.1 larger than that reported by *Cox and Munk* [1954]).

[29] The final step, which consists of deriving U from lidar-derived $\hat{\rho}$, is not trivial because $\hat{\rho}$ is the sum of two compensating terms, ρ_1 and ρ_2, that both depend on U as

$$\rho_1 = (1 - W)\frac{\rho_o}{4\langle S^2 \rangle}, \tag{6}$$

whose dependence on U is given by equation (4), and the modeled dependence of foam reflectance calculated as [*Koepke*, 1984]

$$\rho_2 = \rho_{f,eff} W, \tag{7}$$

where the fractional area covered by whitecaps W can be expressed as a power law of U. Hence, the reflectance due to the slope distribution of the capillary-gravity waves (ρ_1) decreases with increasing SWS, whereas the reflectance due to the slope distribution of the capillary-gravity waves (ρ_2) increases with increasing SWS.

[30] Figure 2 shows the evolution of the SSR (i.e., $\rho_1 + \rho_2$) as a function of U. It also illustrates the sensitivity of the SSR to (1) atmospheric stability conditions and (2) the relationship between SWS and whitecap coverage. Here, we have considered two types of stability conditions: the slightly stable conditions experienced by *Cox and Munk* [1954] (i.e., $\langle S^2 \rangle$ given by equation (3)) and the unstable conditions experienced on 24 March 1998 (i.e., $\langle S^2 \rangle$ given by equation (4)). Two types of whitecap coverage dependence on SWS have also been considered: the relationship established on 24 March 1998 using a combination of digital images of the sea surface made from the Research Vessel Atalante and wind speed measurements made on the ship, based on the technique described by *Dupuis et al.* [1993], yielding

$$W = 1.57\ 10^{-6}\, U^{2.16} \tag{8}$$

and the relationship of *Monahan* [1986]

$$W = 3.84\ 10^{-6}\, U^{3.41}. \tag{9}$$

[31] In Figure 2, the 4 curves correspond to:

1. Curve 1: the wind-waves contribution representative of the average unstable conditions experienced on 24 March 1998 along leg AF, i.e., for a negative stability correction term equal to −1.7, and the foam related reflectance computed using the whitecap coverage dependence on surface wind speed established on 24 March 1998,
2. Curve 2: same as curve 1, but for the slightly stable conditions encountered by *Cox and Munk* [1954],
3. Curve 3: same as curve 1, but for the whitecap coverage dependence on surface wind speed established by *Monahan* [1986],
4. Curve 4: same as curve 2, but for the whitecap coverage dependence on surface wind speed established by *Monahan* [1986].

[32] For the range of SWSs considered here (i.e., 0−30 m s^{-1}), the foam related reflectance obtained from equation (8) is negligible (curves 1 and 2), and the total reflectance

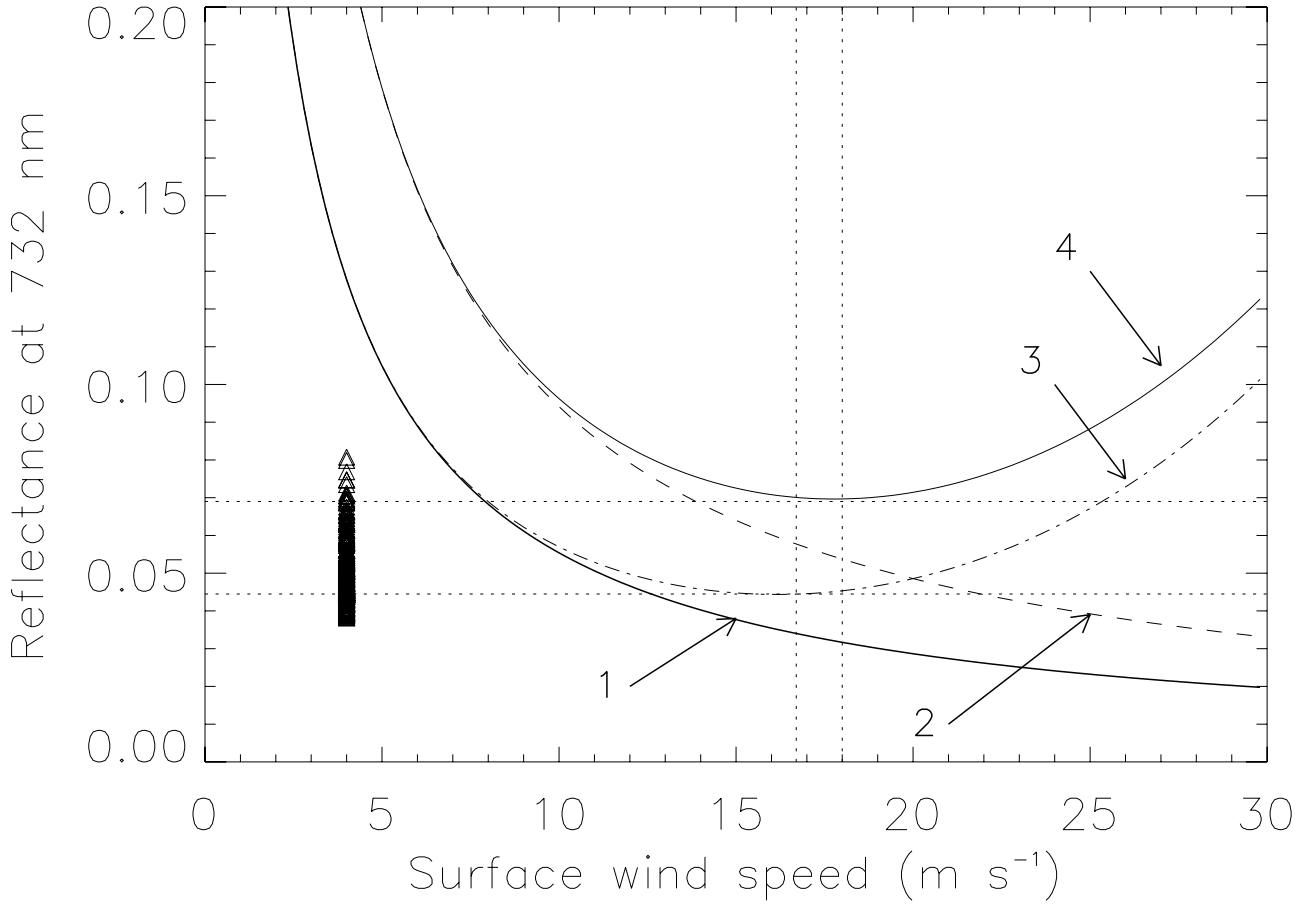

Figure 2. Dependence of the total reflectance (i.e., wind-waves and foam) as a function of surface wind speed. Solid line (1): The wind-waves contribution is representative of the average unstable conditions experienced on 24 March 1998 along leg AF, i.e., for a negative stability correction term equal to −1.7, and the foam related reflectance is computed using the whitecap coverage dependence on surface wind speed established on 24 March 1998. Dashed line (2): same as curve 1, but for the slightly stable conditions encountered by *Cox and Munk* [1954]. Dot-dashed line (3): same as curve 1, but for the whitecap coverage dependence on surface wind speed established by *Monahan* [1986]. Dot-dot-dot-dashed line (4): same as curve 2, but for the whitecap coverage dependence on surface wind speed established by *Monahan* [1986]. The range of SSR reflectance measurements derived from lidar data along leg AF is shown as triangles (they are plotted for a given, fictitious wind speed of 4 m s^{-1}). The vertical dotted line indicates the SWS (noted U_0) corresponding to $\partial\rho/\partial U = 0$, where ρ and U are the modeled reflectance and surface wind speed for curves 3 and 4 (i.e., 16.8 and 18 m s^{-1}, respectively). The horizontal dotted line indicates the SSR corresponding to U_0 (i.e., 0.044 and 0.066 for curves 3 and 4, respectively).

decreases continuously with increasing wind speed. As a result, the contributions ρ_1 and ρ_2 can be separated adequately for each lidar-derived reflectance measurement (shown as triangles) and SWS obtained unambiguously from curves 1 or 2 shown in Figure 2.

[33] When using equation (9), the foam related reflectance is no longer negligible for SWS larger than ≈15 m s^{-1} (curves 3 and 4), and the total reflectance exhibits the general characteristics of a parabola: there exists a threshold value of SWS separating the wind-driven-wave -dominated regime and the whitecap-dominated regime. The threshold values are equal to 16.8 and 18 m s^{-1} for curves 3 and 4, respectively. Even in this case, provided that along leg AF the SWSs were less than 15 m s^{-1} (as indicated by TOPEX measurements, for example), ρ_1 and ρ_2 can be separated and the SWS obtained unambigously from total reflectance curve shown in Figure 2 because we only have to consider the leftmost branch of the curve. Nevertheless, SWS values cannot necessarily be derived for each lidar reflectance measurements because there exist a minimum SSR value (defined by $\partial\rho/\partial U = 0$) associated with the SWS threshold value. In the case of curve 3, no SWSs can inferred from lidar-derived surface reflectance values less than 0.044 (i.e., 61 out of 288 reflectance retrievals along leg AF). In the case of curve 4, no SWSs can inferred from lidar-derived surface reflectance values less than 0.066 (249 out of 288 reflectance measurements). In this case, when considering the uncertainty on lidar-derived SSR (of the order of 10%, see Appendix B), even fewer SWSs can be inferred from lidar data.

[34] In Figure 3, we show the evolution with fetch of the lidar-derived SWS obtained from the 4 curves discussed above. Also shown is the SWS measured at 7 m ASL by the ASIS buoy at 1634 UTC. One may note that lidar-derived SWSs are larger in the slightly stable case than in the

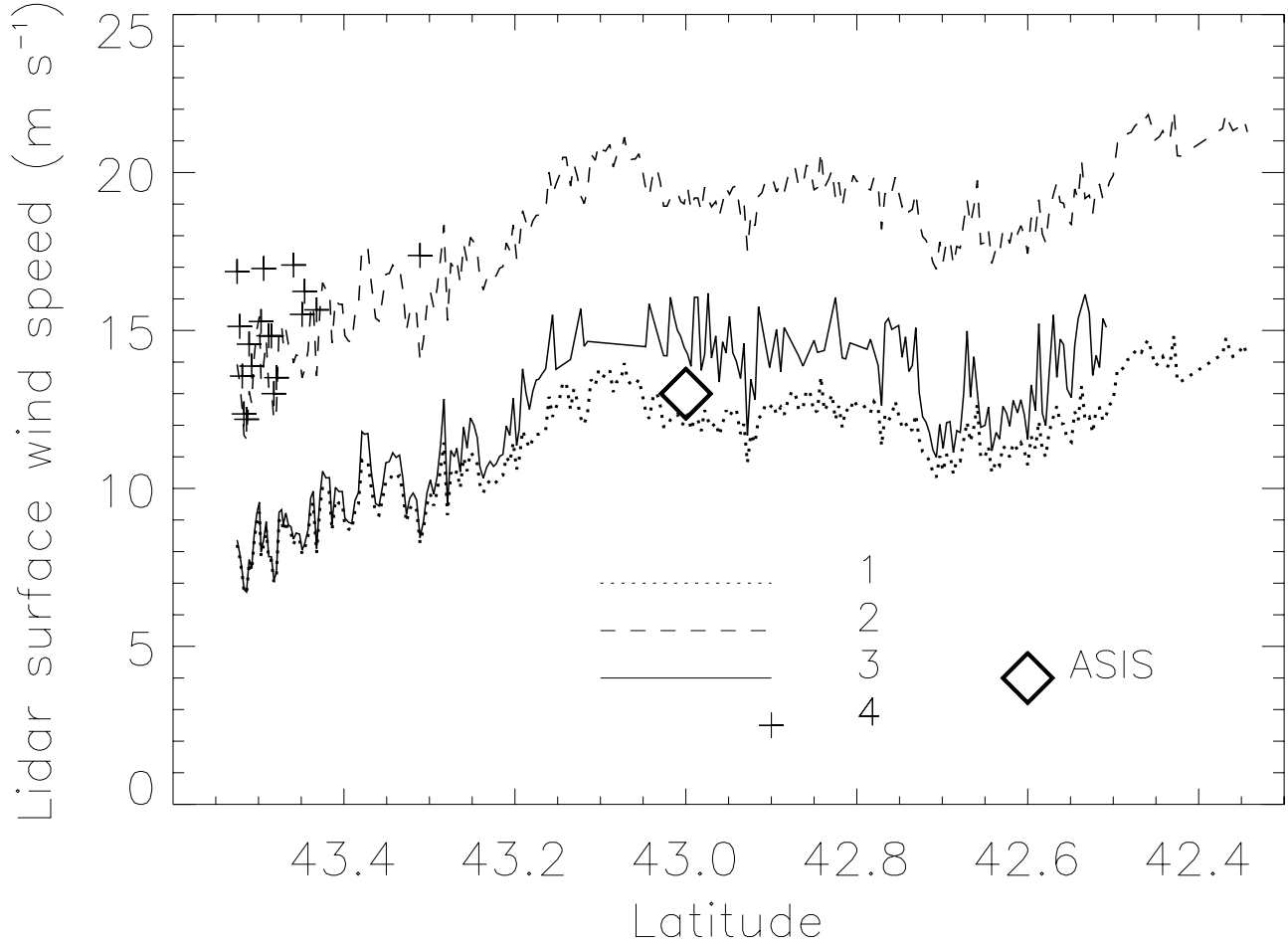

Figure 3. Evolution of lidar-derived SWS with latitude along leg AF for different atmospheric stability conditions and different whitecap coverage dependence on SWS. The labels "1", "2", "3" and "4" correspond to those defined in Figure 2. The diamond corresponds to the ASIS measurement at 1634 UTC.

unstable case. This is due to the higher modeled surface reflectance obtained in stable conditions as illustrated by curve 2 in Figure 2. The agreement between the ASIS measurements and the SWS retrievals in unstable conditions (curve 1) is very good. Hence, there is evidence that the negative stability conditions should be accounted for. Ignoring the stability correction term (i.e., assuming the conditions to be quasi-neutral), the SWS would be $\approx$6.7 m s^{-1} larger on average, along leg AF. In the remainder of this paper, the SWS have been derived from lidar measurements accounting for the unstable atmospheric conditions.

[35] In unstable conditions, the choice of the fractional whitecap coverage dependence on U has an impact on the lidar retrievals for $U > 12$ m s^{-1} only (see the difference between curve 1 and curve 3). For lidar-derived surface reflectance values greater than 0.044, the larger SWSs obtained from curve 3 than from curve 1 for U between 10 and 16.8 m s^{-1} result from the weaker dependence of ρ on U. Given the uncertainty on lidar-derived SSR (Appendix B) and given that the ASIS derived SWS at the time of the ARAT overflight (1634 UTC) falls between the 2 curves, we have no mean of assessing which of the 2 W versus U relationships presented earlier best represents the conditions of the experiment. In the following, we have chosen to use the relationship derived on 24 March 1998 (equation (8)) because it enabled the retrieval of a SWS value for each of the lidar-derived SSR and because the lidar-retrievals were in slightly better agreement with the ASIS measurement. The uncertainty introduced (i.e., by using equation (8) rather than equation (9)) increases exponentially with SWS, but remains below 20% for SWS less than 15 m s^{-1}. It is less than 3% for SWS less than 10 m s^{-1}.

[36] The uncertainty on the so-retrieved SWS is taken as the quadratic sum of three terms: (2) the error associated with the uncertainty on the stability correction term (1.7 ± 0.1) which is on the order of 12%, (2) the error on the near surface backscatter coefficient (10%), and (3) the uncertainty resulting from the natural variability associated with the data, which is calculated as the standard deviation of the SWS computed for each individual profile (prior to the 20 lidar shots average). The natural variability was observed to be quite significant, on the order of 20%. Hence, the total uncertainty associated with the SWS retrievals is equal to 25%.

3.3. Momentum Flux Related Variables From Lidar and Radar Measurements

[37] As mentioned in the introduction, very little has been done on the study of momentum transfer evolution with fetch in offshore conditions. In this paper, we would like to take

advantage of the combination of radar and lidar measurements to do this. In the following, we first discuss the retrieval technique used to determine the surface roughness length (SRL), z_o. Using these retrievals, we then determine the neutral drag coefficient at 10 m ASL. From a combination of neutral drag coefficient and SWS at 10 m ASL, we are able to determine the friction velocity, using a bulk formula.

[38] *Donelan* [1990] has proposed a relationship for dimensionless roughness that accounts for wave age dependence over pure wind sea, of the form

$$\frac{z_o}{\sigma} = A\left(\frac{U_{10N}}{C_p}\right)^B, \tag{10}$$

where σ is the equal to a quarter of the significant wave height, H_s. (C_p/U_{10N}) is referred to as the wave age and C_p is the wave phase velocity, U_{10N} is the SWS at 10 m ASL under neutral conditions. A and B are constants. On 24 March 1998, ASIS data between 1200 and 2400 UTC yield values of A and B equal to 10^{-5} and 7, respectively. The uncertainties associated with C_p and H_s are on the order of 10 to 15%. Note that for these data, the coefficients A and B are significantly different from those derived using a composite of 5 data sets, including FETCH [cf. *Drennan et al*. [2003]]. With these composite data, $A = 7\ 10^{-4}$ and $B = 2.8$. The data from 24 March, 1200–2300 UTC, have significantly lower roughness lengths than the remainder of the FETCH data. In fact, the 24 March data from 1450 to 1620 UTC have been excluded from the data set used by *Drennan et al*. [2003] to derive their relationship because the points did not meet the rough flow criterion ($z_o u^*/g > 2.3$). We thus have treated the 24 March 1998 data as a special case, using equation (10) with the regression coefficients determined from those data alone.

[39] z_o is obtained from measurements of the SWS made by LEANDRE 2 and sea state characteristics made by RESSAC (σ and C_p) along leg AF. The wave phase velocity along AF is calculated from the wave peak frequency, f_p, measured by radar using the wave dispersion relationship for infinite water depth (the water depth at the location of the RESSAC measurements along AF is estimated to be at least 35 m) as

$$C_p = \frac{g}{2\pi f_p}. \tag{11}$$

[40] U_{10N} is obtained from the lidar-derived SWS, U, using the flux profile relations, $\psi_u(z/L)$, from *Donelan* [1990]

$$U_{10N} = U(z) + \left(u_*/\kappa\right)\psi_u(z/L), \tag{12}$$

where κ is the von Karman constant (0.4), ψ_u is a stability function defined as [*Dyer*, 1974]

$$\psi_u(z/L) = 2\ln((1+\phi_u)/2) + \ln\left((1+\phi_u^2)/2\right) - 2\arctan\phi_u + \pi/2, \tag{13}$$

with

$$\phi_u = (1 - 16(z/L))^{0.25}, \tag{14}$$

and L is the Obukhov length given by

$$L = -u_*^3\left[\kappa g/\rho\left(H/\left(c_p\theta_0\right) + 0.61E/L_v\right)\right], \tag{15}$$

with ρ is the density of air, E and H the latent and sensible heat flux, c_p the specific heat at constant pressure, L_v the latent heat of vaporization, u_* the friction velocity and θ_0 is the reference potential temperature. First guess values of L and u_* were derived from ALADIN 1800 UTC forecast outputs (13 model points along leg AF) interpolated at the position of each lidar SWS estimate. The correction term (i.e., the second term on the right hand side of equation (12) amounted to 0.3 ± 0.1 m s^{-1}, on average, along leg AF.

[41] The neutral drag coefficient is then obtained from lidar/radar measurements as

$$C_{10N} = \kappa^2[\log(z/z_o)]^{-2}, \tag{16}$$

and the friction velocity is obtained as

$$u_* = \sqrt{C_{10N}}U_{1ON}. \tag{17}$$

4. Results

[42] In this section, we discuss the evolution of MSS, SWS and SRL with fetch as obtained from the different platforms along leg AF. The comparison was complicated by (1) the fact that the measurements from the different platforms were not made simultaneously in the same location and (2) the nonstationary nature of the Mistral flow over the GoL on 24 March 1998 (see section 2). Hereafter, we begin with a description of the spatiotemporal evolution of the atmospheric forcing and its impact on sea state.

4.1. Nonstationary Aspect of the Mistral Flow Between 1500 and 2100 UTC

[43] Figure 4 presents the ALADIN wind field at 10 m ASL over the GoL on 24 March 1998 at 1500, 1800 and 2100 UTC. An important feature associated with cold-air outbreaks over the GoL is observed in the form of banners of weaker winds (sheltered region) shown as regions where the SWS is less than 10 m s^{-1}.

[44] At 1500 UTC, a region of wind speeds less than 10 m s^{-1} was observed in the eastern part of the domain, which corresponds to the sheltering region (associated with the Maritime Alps) separating the Mistral from the outflow from the Gulf of Genova (Figure 4a). As a result, the Mistral appeared to lose its characteristics over the Sea, the largest winds associated with the mistral now being observed over the continent, in the Rhone Valley. At 1800 UTC, the Tramontane flow was observed to be shifted to the southwest as the Mistral began to intensify again. The influence of the sheltered region to the east of the Mistral also appeared to weaken. The sheltered region separating the Mistral and the Tramontane was very narrow at that time (Figure 4b). The cold and jet-like characteristics of the Mistral were only maintained over the continent and were rapidly lost over the sea. Finally at 2100 UTC, the Mistral flow was well established again. It had a more marked northerly direction than at 1200 UTC due to the southward displacement of the Alpine lee cyclone (Figure 4c) [*Flamant*, 2003].

4.2. Sea State

[45] Nondirectional spectra from 24 March 1998 are plotted for four locations from the shore to open sea (Figure 5) respectively at 50, 75, 95, and 115 km of fetch distance

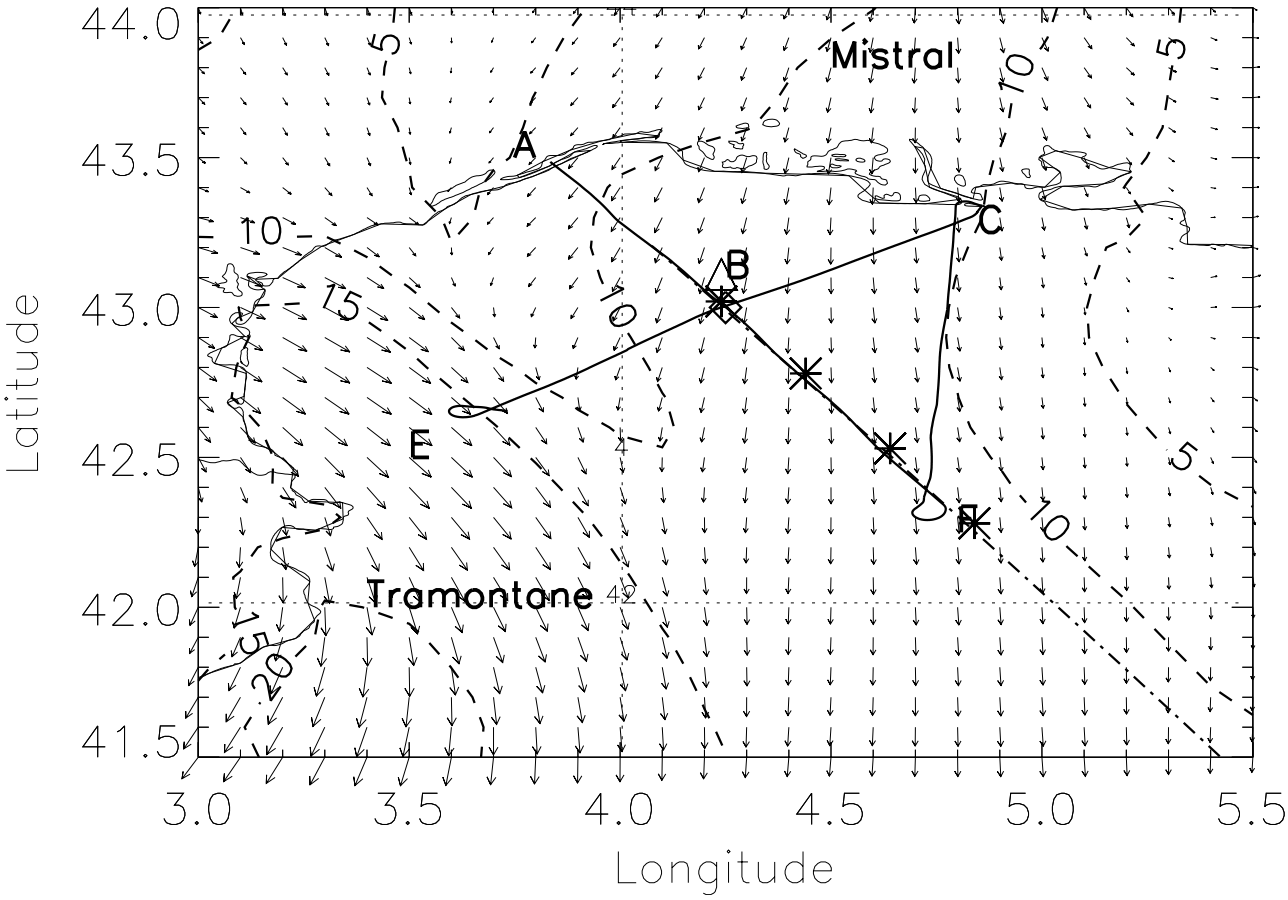

Figure 4. Wind fields simulated in the ABL (at 10 ASL) on 24 March 1998 by the French operational forecast model ALADIN at (a) 1500, (b) 1800 and (c) 2100 UTC. The diamond (triangle) corresponds to the position of the ASIS buoy (Atalante). Superimposed are isotachs between 10 and 20 m s^{-1} with 5 m s^{-1} increments. Also superimposed are the ARAT flight tracks corresponding to afternoon flights. The rugged solid line represents the coastline The asterisks indicate the position of the 1-D spectra shown in Figure 5.

calculated as the distance from the coast assuming the wind to be northerly as shown by ALADIN model (see the location of the spectra in Figure 4). The spectra behaved as expected for limited fetch situations, i.e., they exhibited an increase of the energy and decrease of the peak frequency for increasing fetch distance. The peak frequency evolves with fetch as predicted by the JONSWAP relationship [*Hasselmann et al.*, 1973] for a wind speed of the order of 15 m s^{-1}, although the significant wave height increase more rapidly than with the JONSWAP relationship.

[46] Analysis of the wave directional spectra showed a marked swell component in the southern part of the track. For the same four locations, the normalized energy density (with respect to the peak) are plotted with contour levels in Figure 6. The ambiguity in the direction of RESSAC spectra was resolved with the output of the numerical sea state prediction model, WAMMED coupled with ALADIN 10 m ASL winds. WAMMED is the ''Mediterranean version'' of the operational WAM wave prediction model at ECMWF (European Center for Medium-range Weather Forecasts) [*Bidlot*, 2001, available at http://www.ecmwf.int/publications/newsletters/list.html] which provides routinely the directional wave spectrum at a 0.25° × 0.25° resolution, and uses as input the wind field of the ECMWF global atmospheric model IFS (Integrated Forecast System). Here a research version of WAMMED was used: the resolution was increased to 0.083° × 0.083° in latitude/longitude and the wind-forcing was provided by ALADIN at the same resolution. The directions refer to waves going to. For the locations 1 and 2, directional spectra were bimodal, the two peaks of similar frequency propagating on both sides of the wind direction (northerly). These waves are recognized as being generated by the action of the Mistral. At locations 3 and 4, three wave components were observed. One was propagating to the south and was identified as a Mistral generated wave train. The second component was propagating at lower frequency to the south-east and resulted from the action of the Tramontane blowing to the west of the region of operation. The last component with the lowest frequency was propagating to west-southwest. Theses waves were related to swell advecting from the Ligurian sea (as discussed above on the basis of ALADIN forecasts, Figure 4) and contributed up to one third of the total wave energy at the location 4.

[47] In the northern part of the track (north of 42.75°N), sea-state is dominated by the Mistral flow and is limited in

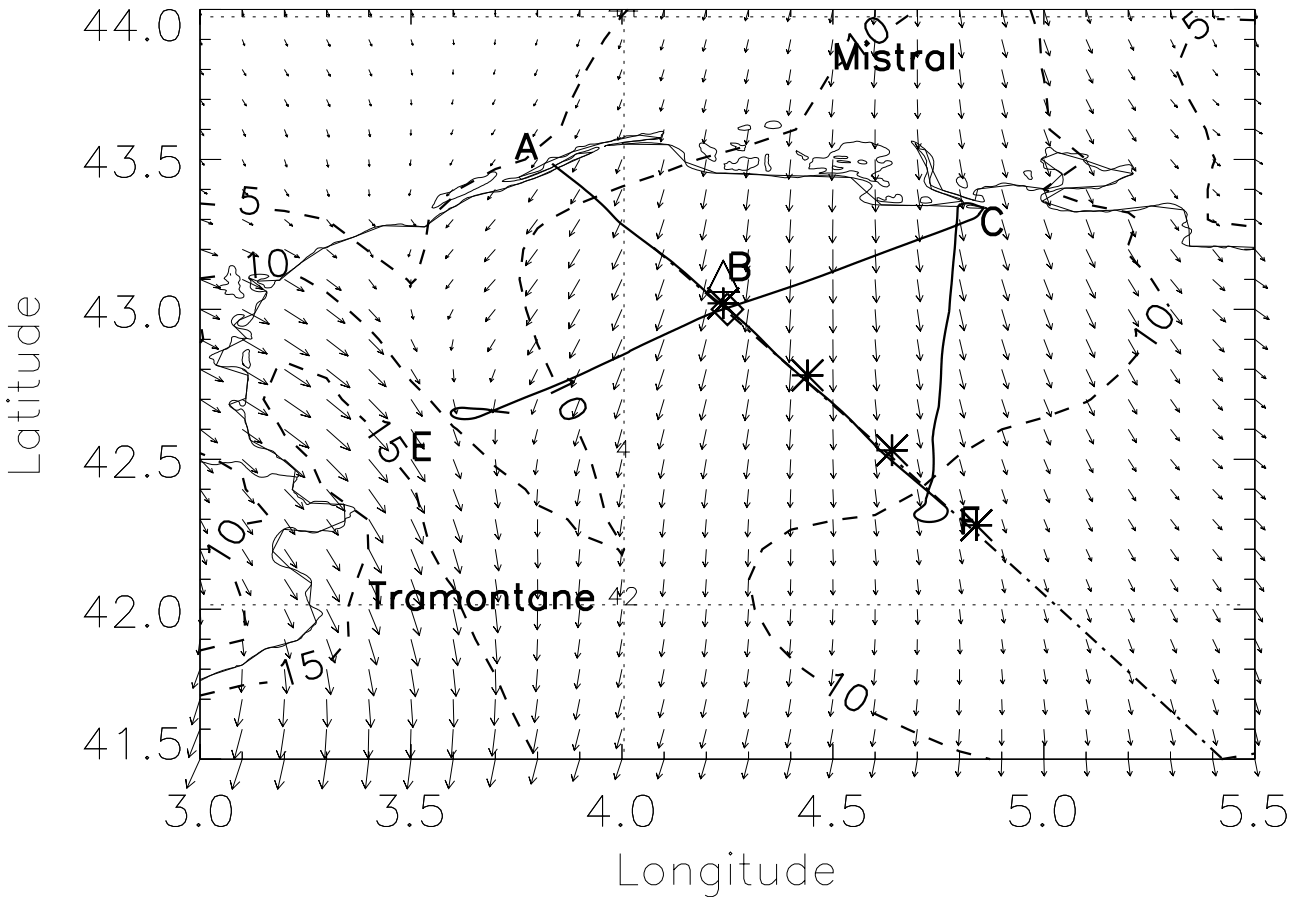

Figure 4. (continued)

fetch. In the southern part of the track, the wave energy grows not only due to the wind wave evolution with the fetch laws, but also with the swell contribution. Only 80% of the significant wave height is related to wind sea in that region.

4.3. Evolution of Radar, Lidar, and TOPEX Mean Square Slopes With Fetch

[48] The evolution of lidar- and radar-derived (C-Band and Ku-Band) MSS as a function of the distance to the coast on leg AF is shown in Figure 7. Radar (TOPEX and RESSAC) MSS are obtained according to the methodology presented in Appendix C. The lidar-derived MSSs are obtained from equation (2) assuming the foam contribution can be neglected in the 24 March 1998 case (see discussion in section 3.2). The largest (smallest) MSSs were obtained from lidar (radar C-Band) measurements. This is related to the wave number interval over which the energy spectrum is integrated to yield the MSS (i.e., $\langle S^2 \rangle \approx \int k^2 S(k)\, dk$, where $S(k)$ is a function describing the evolution of the wave energy as a function of wave number k). The wavelength interval to which instruments are sensitive is defined by the wavelength of operation (lower limit) and the footprint (upper limit). The wavelength intervals (in m) of LEANDRE 2, TOPEX KU-Band, TOPEX C-Band and RESSAC are [0, 9], [0.08, 10000], [0.2, 10000] and [0.2, 500], respectively. The corresponding wave number intervals (in m^{-1}) are [0.7, ∞], [6 10^{-3}, 80], [6 10^{-3}, 30] and [0.01, 30], respectively. Hence, the larger MSS derived from lidar measurements reflect the fact that the energy spectrum is integrated (1) over a wider wave number range and (2) in a region of the spectrum sensitive to k^2. Due to the smaller footprint, lidar-derived MSS exhibits a greater variability than its radar counterparts. Nevertheless, the 4 curves exhibit very similar trends as a function of latitude: first, a MSS steadily increasing with decreasing latitude (increasing distance from the coast) between the coast and 43°N, then a sharp decrease in MSS followed by a relatively constant MSS (43–42.6°N) and finally a MSS increasing again with the distance from the coast (42.6–42.4°N). The increase in the 42.6–42.4°N region is thought to be related to the presence of swell coming from the Gulf of Genova and cannot solely be interpreted in terms of SWS (i.e., the influence of swell has been discarded from the data used by *Cox and Munk* [1954] to establish the empirical relationship given by equation (3)). Radar data also showed that the MSS increased before stabilizing further away from the coast.

4.4. Evolution of Surface Wind Speed With Fetch

[49] The evolution of lidar-derived SWS as a function of the distance from the coast on leg AF (12 m ASL, between 1620 and 1640 UTC) is illustrated in Figure 8. It is compared to the SWS simulated by ALADIN (10 m ASL, at 1800 and 2100 UTC), and to measurements made by ASIS and on-board the Atalante (7 and 17 m ASL, respectively, at 1600 and 1700 UTC) as well as by TOPEX (10 m, at 1844 UTC) and in situ measurements performed from the ARAT (between 1750 and 1850 UTC) at 100 m ASL and at 300 m ASL (leg FB and leg BA, respectively, see Figure 1).

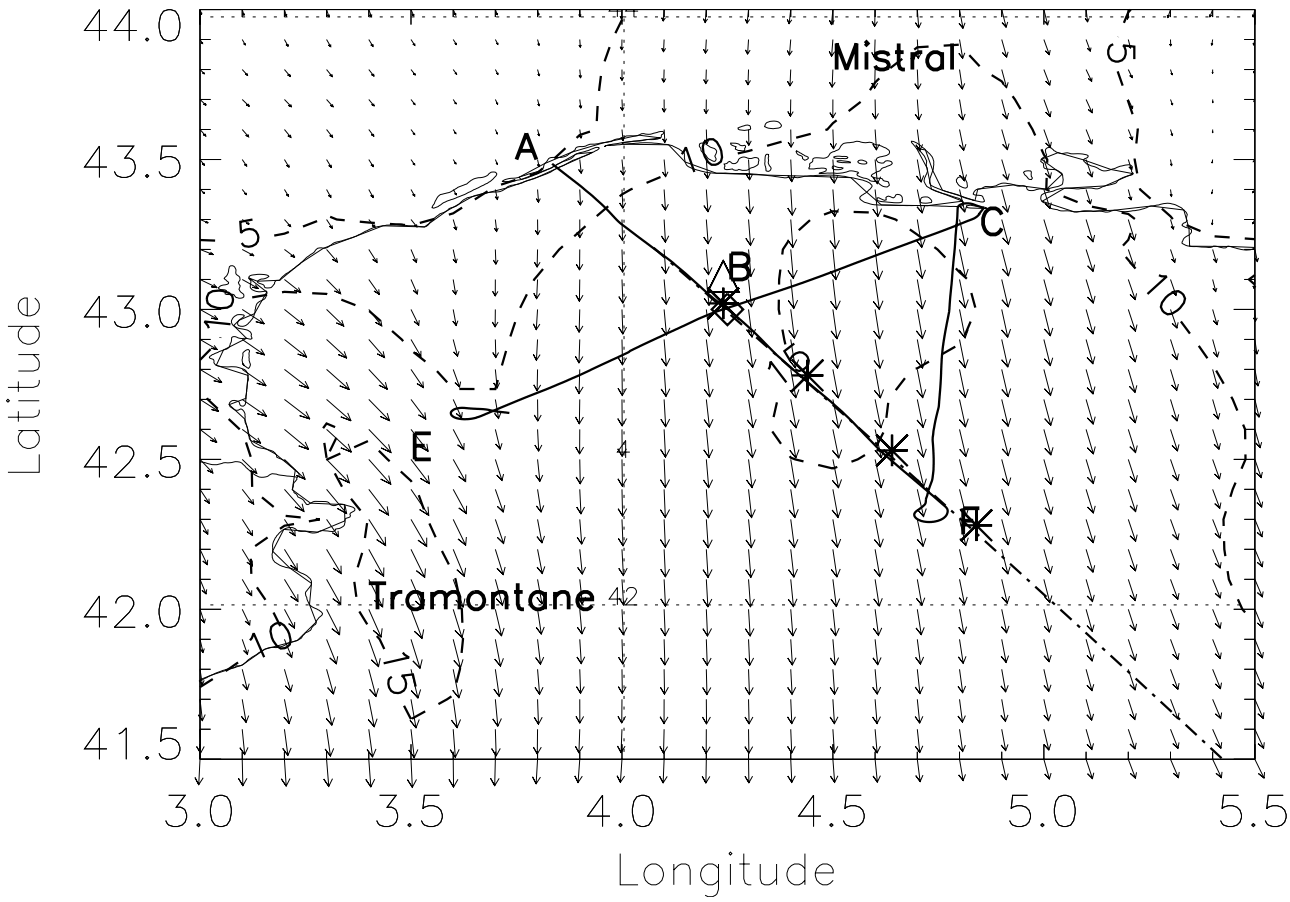

Figure 4. (continued)

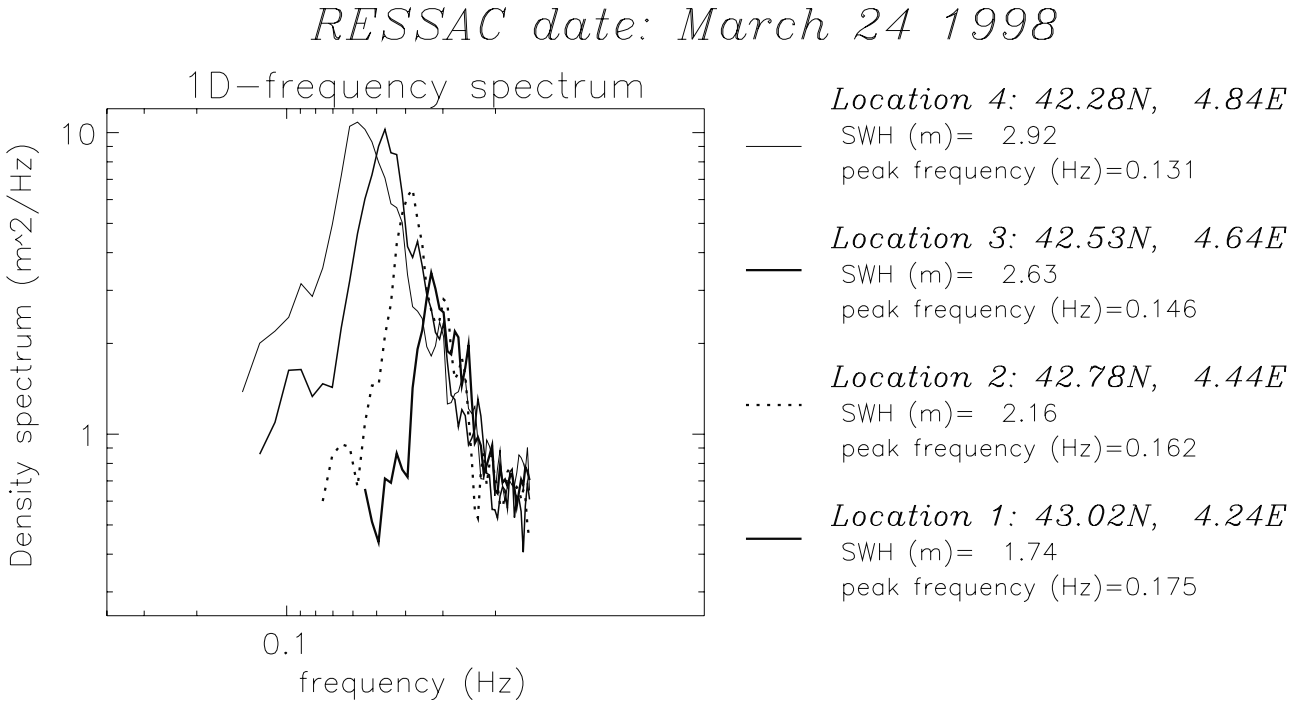

Figure 5. One dimensional spectra obtained from RESSAC at four locations: (1) near the shore in thick solid line, (2) in dotted line, (3) in dash-dotted line, and (4) in open sea in thin solid line. The energy density spectrum is plotted in log-log scale. The horizontal axis is for the frequency (Hz).

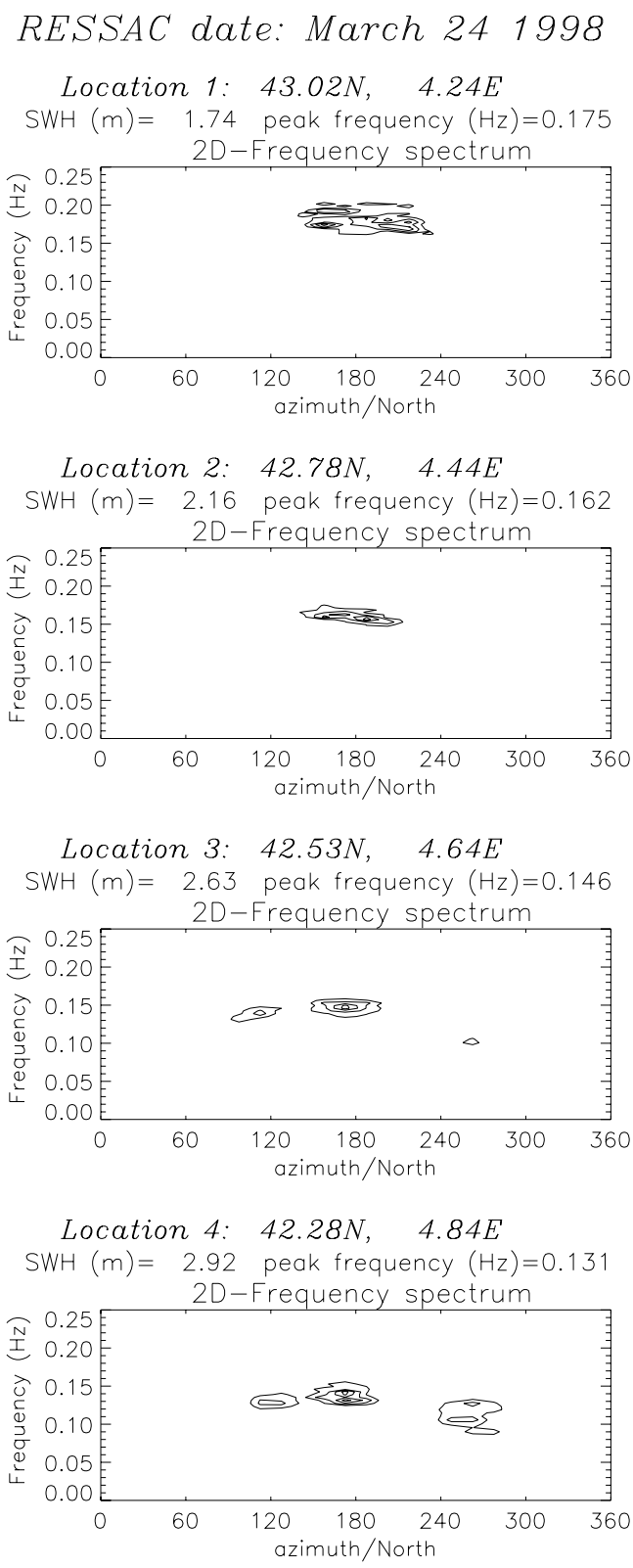

Figure 6. Two dimensional spectra obtained from RESSAC at four locations from the shore to open sea. The normalized energy density (with respect to the peak) is plotted with contour levels of 0.3, 0.5, 0.7, and 0.9. The horizontal axis gives the azimuth (from true North). The vertical axis is for the frequency (Hz). The directions refer to waves going to.

TOPEX SWS are estimated from the normalized radar cross section according to a model function defined by the modified Chelton and Wentz algorithm [*Witter and Chelton*, 1991]. The model function used here is a least squares fit of a fifth order polynomial to the tabular model of *Witter and Chelton* [1991]. The comparison was made regardless of the height ASL at which the measurements are made.

[50] Between 43.5–43.1°, lidar SWS increases as a function of the distance from the coastline. Such increase is not unexpected and is due to the acceleration of the flow associated with the land/sea roughness transition. However, it is further amplified by the presence of the sheltered region (characterized by weak winds) in the lee of the Massif Central (Figure 4b). In other terms, in the absence of such a feature, lidar SWS increase might not have been as pronounced. This behavior is in good agreement with the ALADIN SWS obtained from ALADIN at 1800 UTC.

[51] Between 43.2 and 42.8° (the core of the "perturbed" Mistral flow [*Flamant*, 2003]), the lidar SWS was relatively constant (12–13 m s^{-1}). The agreement with ASIS SWS (at 1600 and 1700 UTC) and TOPEX SWS was good. ALADIN SWS at 1800 UTC also were in excellent agreement with observations. At 43.1°, lidar SWS and ALADIN SWS are in good agreement with Atalante SWS at 1700 UTC. The Atalante SWS at 1600 UTC was 2.5 m s^{-1} lower than at 1700 UTC. Such a trend as also been observed for the ASIS SWS, though not as marked (i.e., a 1 m s^{-1} increase was observed between 1600 and 1700 UTC). It is thought to be related to the nonstationary aspect of the Mistral flow over the GoL as well as the important spatial variability in the wind field due to the presence of a drifting sheltered region and low-level jets. ASIS and Atalante SWS measurements both showed a minimum in wind speed at approximately 1600 UTC, corresponding to the perturbed Mistral period [*Flamant*, 2003].

[52] Between 42.8–42.5°, lidar SWS were observed to decrease by as much as 3–4 m s^{-1}, before increasing back to values around 15 m s^{-1} (in connection with the presence of swell), these latter values being in agreement with TOPEX SWS retrievals. Note that this region of weaker winds was also observed in the ARAT SWSs, so that it is not believed to be due to errors in the correction of atmospheric effects (changes in aerosol optical properties for example) in the lidar SWS retrieval procedure. Interestingly, ALADIN SWS also decreased substantially between 42.8–42.5°. However, ALADIN SWS kept on decreasing south of 42.5°. This decrease was interpreted by *Flamant* [2003] as the signature of a sheltered region in the lee of the Maritime Alps resulting from the interaction of the northeasterly synoptic winds and the obstacle. ALADIN SWSs at 2100 UTC also showed that this feature had moved eastward as the Mistral became well established again. Hence, the picture arises that ALADIN might not have captured all the spatial variability associated with features such as sheltered regions.

[53] Even though substantially larger, ARAT SWSs (at 100 and 300 m ASL) exhibited a trend similar to lidar SWSs, i.e., steadily increasing winds with fetch, a region of lighter winds and stronger winds again. The region of decreasing winds however was located slightly to the north of that observed in the near surface winds. This is consistent with the analysis of *Flamant* [2003] who showed that the flow at 300 m was more perturbed by the outflow coming

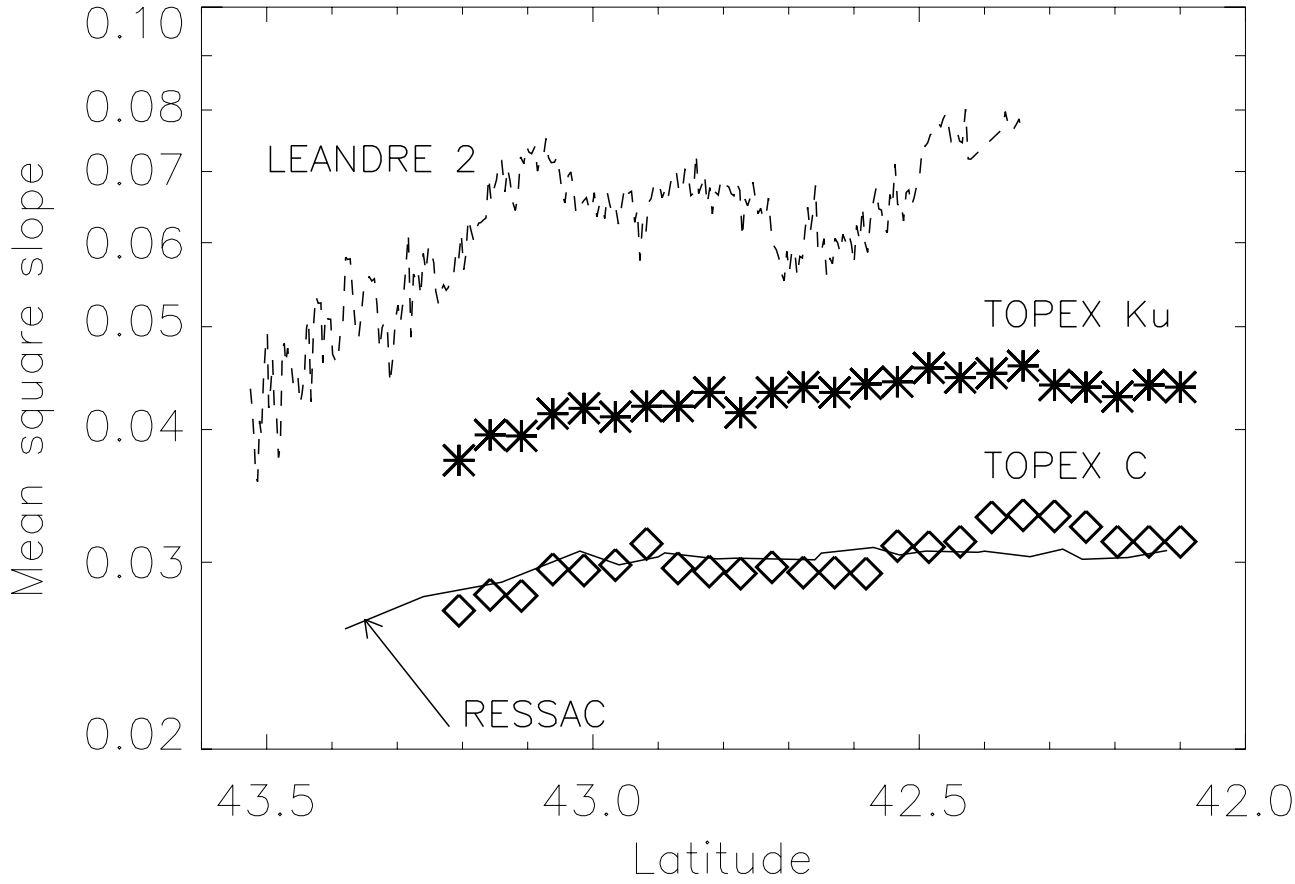

Figure 7. LEANDRE (dashed line), RESSAC (solid line) and TOPEX (diamonds and asterisks for C-Band and Ku-Band, respectively) MSS measurements along leg AF.

from the Ligurian sea than at the surface. Hence, the location of the sheltered region was shifted to the northwest by the stronger outflow at 300 m.

[54] TOPEX SWSs were acquired later than any of the other measurements, during a period where the Mistral was no longer perturbed by the outflow from the Ligurian Sea as the cyclone was moving southward. The steadily increasing winds measured by TOPEX most likely revealed that the Mistral was well established again at the time of overpass. *Flamant* [2003] has shown that the 1800 UTC ALADIN forecast compared well with the measurements made between 1600 and 1700 UTC. Therefore, even though TOPEX measurements were made at a time close to the ALADIN forecast shown in Figure 8, it is not so surprising to find that these retrievals exhibited the largest differences. This is confirmed by good agreement between TOPEX SWSs and ALADIN SWSs at 2100 UTC. Hence the TOPEX overpass occurred at a time when the Mistral was well established again.

4.5. Evolution of Roughness Length With Fetch

[55] Figure 9 shows the temporal evolution of neutral SWS at 10 m ASL, significant wave height and wave phase velocity measured by ASIS between 1200 and 2400 UTC on 24 March 1998. In order to compute the roughness length in such nonstationary meteorological conditions, an attempt was made to correct for the time shift between the lidar and the radar measurements. This correction consisted of 2 steps: (1) because airborne measurements are not made instantaneously on leg AF, a correction was applied for the temporal drift of the variables between the beginning and the end of the leg (40 min and 47 min for LEANDRE 2 and RESSAC, respectively). The drift was computed from ASIS measurements, assuming the temporal evolution observed at this point was representative of that over the entire leg. The drift is null at the time of the aircraft overflight of ASIS (1632 and 1746 UTC for the ARAT and the Merlin, respectively); (2) because airborne measurements are not made simultaneously, the radar-derived C_p and H_s were shifted back 84 min, i.e., from 1746 to 1632 UTC, by increasing C_p by 1.42 m s^{-1} and H_s by 0.05 m.

[56] The evolution of lidar/radar-derived roughness length, z_o as a function of the distance from the coast on leg AF is shown in Figure 10. For comparison, the roughness length derived from ASIS measurements between 1603 and 1733 UTC is also shown. z_o exhibited the same trend as MSS and SWS: first, an increase with the distance from the coast, then a sharp decrease followed by a relatively constant value and finally an increase again with the distance from the coast. Between the coast line and 43.25°N, the increase of z_o is believed to be caused by the sheltering effects in the lee of the Massif Central, and the fact that the lidar documented the transition between sheltered and unsheltered Mistral flow. Between 43.25°N and 43.05°N, we observed an increase of z_o with the distance from the coast line (Figure 10). In this region the wave steepness

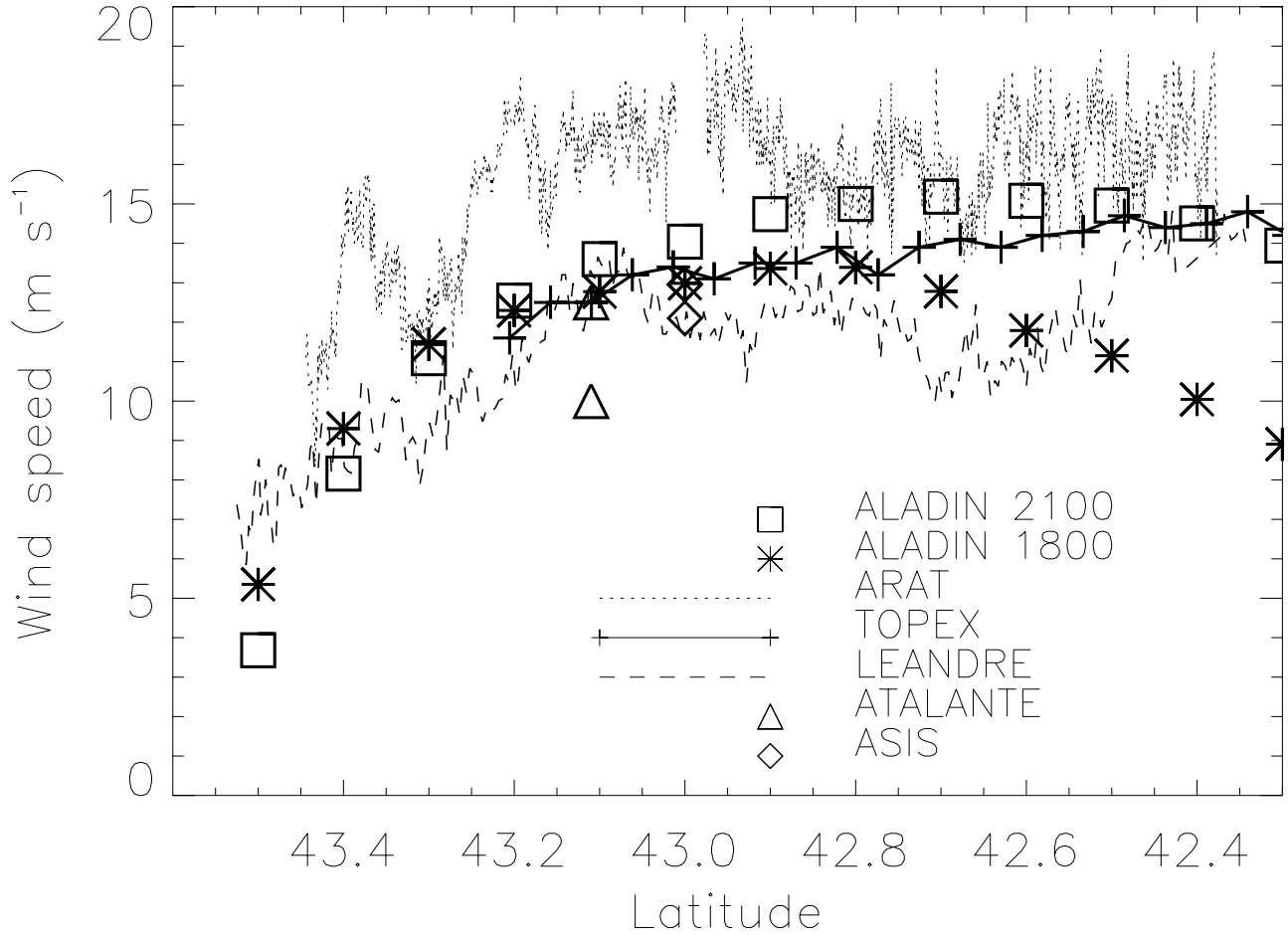

Figure 8. Comparison of sea-borne (7 m ASL, diamonds), ship-borne (17 m ASL, triangles), airborne lidar (12.4 m ASL, dashed line), airborne in situ (100 and 300 m ASL) and spaceborne (10 m ASL, connected crosses) SWS measurements along leg AF with SWS simulated by ALADIN at 1800 UTC (10 m ASL, asterisks) and 2100 UTC (squares).

parameter, H_s/λ_p, was decreasing, indicating the presence of steep, young developing waves. Between 43°N and 42.05°N, H_s/λ_p was observed to be approximately constant, indicating that the sea was fully developed.

[57] ASIS buoy measurements (Figure 10) also show that z_o increased by a factor of 30 between 1603 and 1733 UTC, illustrating the very nonstationary conditions experienced during the operations in the afternoon of 24 March 1998. Another non negligible source of variability for z_o is its great sensitivity to uncertainties on U_{10N}, C_p and σ as well as to the coefficients A and B of equation (10). To illustrate this, we have computed the relative error on z_o resulting from a ±10% uncertainty on the above mentioned variables. For each variable taken separately, the uncertainty of U_{10N} results in the greatest relative error on z_o (i.e., 95%) due to the high value of coefficient B (i.e., 7). For the same reasons, the second largest source of error (i.e., −49%) is associated with the uncertainty on C_p. For randomly distributed uncertainties in the range [−10%, +10%], the relative error on z_o can be huge, i.e., [−75%, +195%].

[58] At the location of ASIS, the lidar/radar-derived z_o was larger than the z_o measured at the buoy at 1632 UTC. This can be explained by the fact that airborne retrievals of C_p, H_s and U_{10N} did not match exactly those of ASIS at 1632 UTC. Nevertheless, one can note the remarkable consistency of the lidar-radar derived z_o, spreading over less than an order of magnitude, when ASIS z_o varied by more than a factor of 30 during the same period.

4.6. Drag Coefficient

[59] In Figure 11, we show the spatial evolution of the neutral drag coefficient derived from combined lidar/radar measurements as a function of the lidar-derived neutral 10 m SWS. Given the sensitivity of C_{dN} to C_p, H_s and U_{10N}, we have normalized the lidar/radar derived z_o to the ASIS-derived z_o at 1634 UTC. Here, we shall only focus on the spatial evolution of the drag coefficient. Given the sensitivity of C_{dN} to remotely sensed variables and the rather large uncertainties (10−25%) associated with these variables, we feel it is illusive to attempt to demonstrate that the drag coefficient can be unambiguously determined from airborne measurements alone.

[60] For comparison, we show the drag coefficients estimated from ASIS measurements between 1603 and 1734 UTC in Figure 11. Note that the inverse wave age corresponding to these points are 0.0468, 0.0545, 0.0616 and 0.0754. We also show, the inverse wave age dependent neutral drag versus wind speed relationships. As in the work of *Drennan et al.* [2003], these relationships are obtained by solving iteratively a set of 3 equations, i.e.,

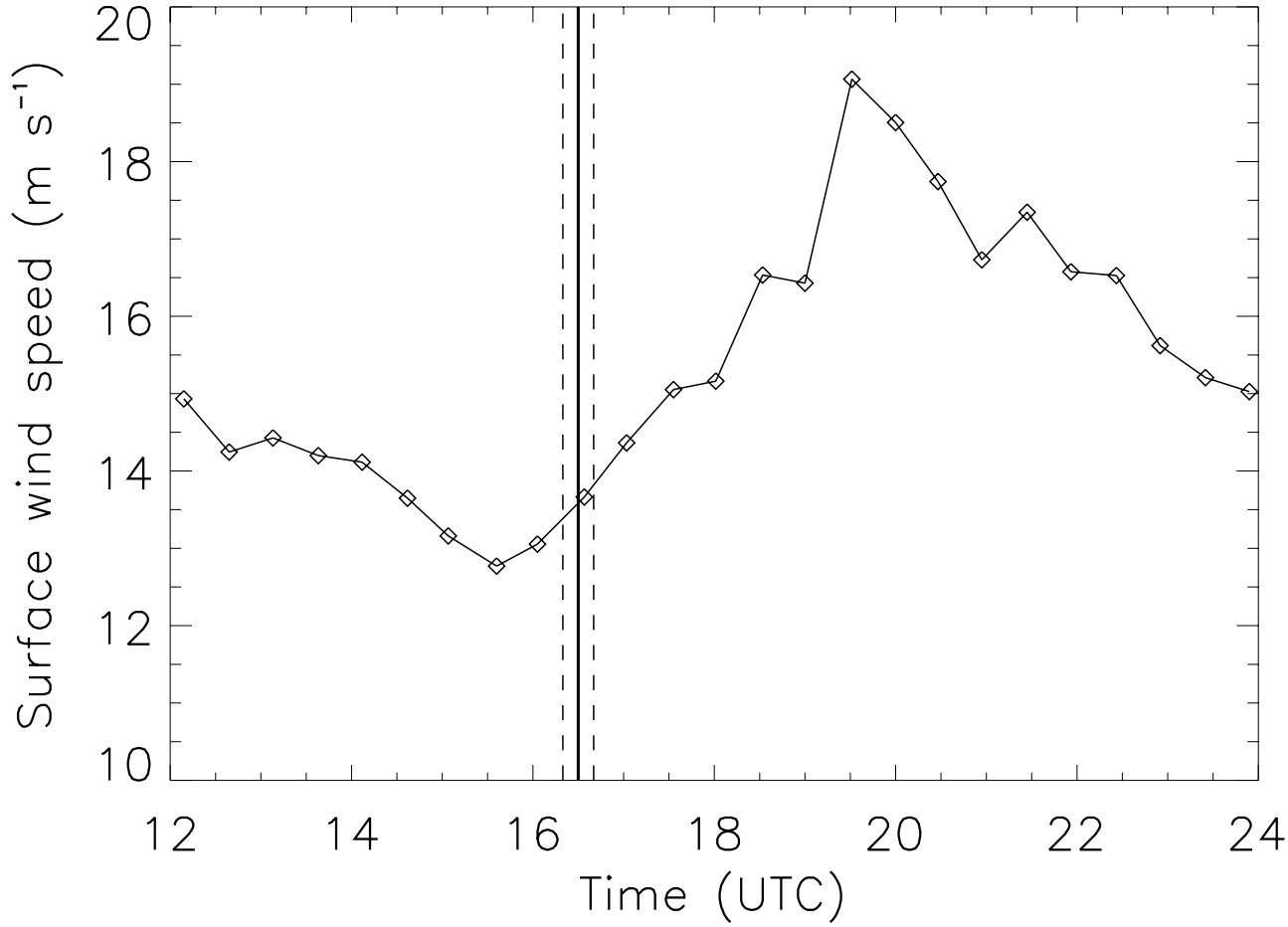

Figure 9. Temporal evolution of (a) neutral SWS at 10 m ASL, (b) significant wave height and (c) wave phase velocity measured by ASIS between 1200 and 2400 UTC on 24 March 1998. For panel (a), the vertical solid line indicates the time of ARAT overflight of ASIS (1632 UTC). The vertical dashed lines on both sides indicate the start and end time of leg AF flown by the ARAT. For panels (b) and (c), the vertical solid line indicates the time of Merlin overflight of ASIS (1746 UTC). The vertical dashed lines on both sides indicate the start and end time of leg AF flown by the Merlin.

equations (16) and (17) and relationship relating the Charnock parameter ($\alpha = z_o g/u_*^2$) to the inverse wave age. The later, obtained on the 24 March 1998 from the ASIS data, yields

$$\frac{z_o g}{u_*^2} = 250\left(\frac{u_*}{C_p}\right)^4. \quad (18)$$

[61] The drag coefficients estimated from combined radar/lidar measurements are observed to correspond to inverse wave age values between 0.05 and 0.07, which is remarkably consistent with the ASIS measurements. For further analysis of the evolution of the drag coefficient with fetch, we have plotted with different colors and symbols the data grouped in the 4 latitudinal ensembles determined from the behavior of the SRL and SWS as a function of fetch: between the coast and 43.25°N (sheltered region, group 1), between 43.25°N and 43°N (developing sea, group 2), between 43°N and 42.7°N (developed sea, group 3) and beyond 42.7°N (swell contamination, group 4). The lidar/radar derived data indicated that younger (older) waves were indeed observed at short (long) fetch. Data from groups 2 and 4 were identified to exhibit less scatter than data from group 1 and 3. The reason for this is believed to that in the corresponding regions, the action of wind on the sea surface was more steady, less perturbed than in the sheltered region (group 1) or at the eastern edge of the Mistral (group 3) where forcing of the wave field is expected to be more transient than in established flow regions. However, the drag coefficient data from groups 2–4, exhibit steeper trends with U_{10N} than those associated with the constant-inverse-wave-age relationships.

4.7. Friction Velocity

[62] In Figure 12, we show the spatial evolution of the friction velocity derived from combined lidar/radar measurements and forecasted by ALADIN (1800 UTC) as a function of latitude. Also shown are the friction velocity derived from ARAT in situ measurements made at 100 m ASL using a eddy-correlation technique between waypoints F and B, as well as the ASIS measurements at 1603, 1634 and 1702 UTC.

[63] The ALADIN and lidar/radar friction velocities at the location of ASIS were found in good agreement with the ASIS measurement at 1634 UTC. Good agreement is also found between in situ aircraft measurements and lidar/radar

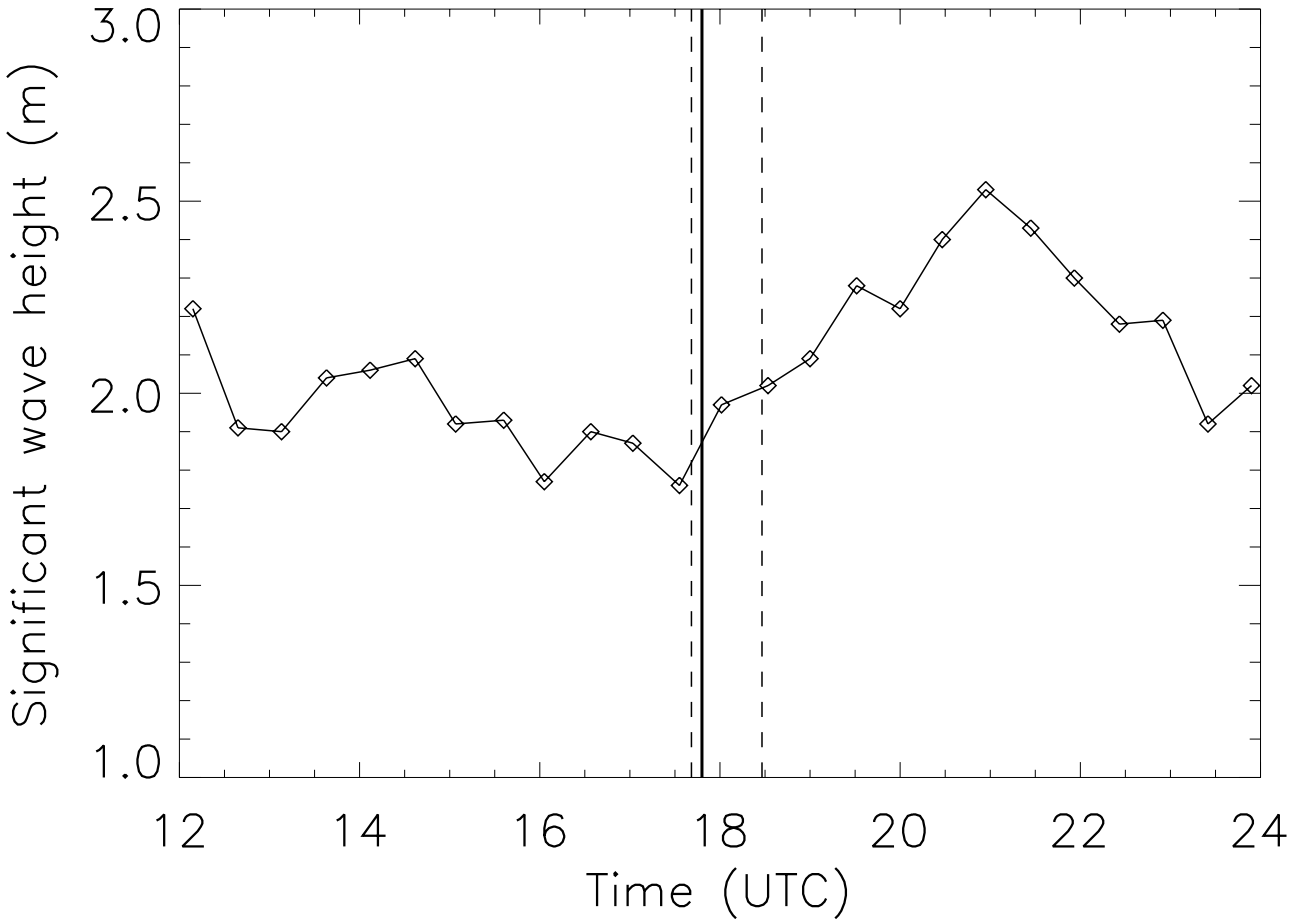

Figure 9. (continued)

retrievals. In particular, remote sensing estimates reproduced the increase of friction velocity near 42.5°N. This increase was not forecasted by ALADIN. ALADIN forecasted an increasing friction velocity between the coast and 43.1°N, and a nearly constant friction velocity further south. Lidar/radar retrievals exhibited a similar trend, but with much more variability.

5. Conclusion

[64] This paper describes a novel approach, using airborne lidar and radar measurements, to determine sea surface variables (sea surface wind, surface roughness length, drag coefficient and friction velocity) and analyze their spatial variability with an unprecedented horizontal resolution. This novel approach was tested in the complex coastal environment of the Gulf of Lion during a Mistral event documented in the framework of the FETCH experiment.

[65] The present study shows that in the coastal environment, and under strong wind, cold-air outbreak type conditions, accurate lidar-derived SWS can be obtained provided that exogenous information on the stability conditions and the whitecap coverage dependence on SWS is available. Stability was shown to be crucial as it could introduce a large bias in SWS retrievals (6.7 m s^{-1} on average on leg AF). Fortunately, this variable can be obtained, with a reasonable accuracy, from numerical weather prediction models. In limited fetch conditions, the knowledge of the whitecap coverage dependence on SWS was found not to be as critical (as that of stability). The impact (or the lack thereof) of the whitecap coverage dependence with SWS on lidar-derived SWS was assessed by comparing results obtained using (1) the *Monahan* [1986] relationship (for fully developed sea conditions) and (2) a relationship determined specifically on 24 March 1998. The knowledge of such a relationship may not be considered a crucial part of laser remote-sensing oriented experiments in coastal regions. Particular attention was given to lidar calibration and inversion approaches to ensure relevant, trustworthy SWS retrieval by lidar. The somewhat tedious processing that needed to be implemented was a direct consequence of the fact that the lidar used in this study was not developed for the primary purpose of measuring SWS. A lidar system specifically developed for the purpose of measuring SWS [e.g., a system with longer wavelength and multiple look angles] would alleviate some of the limitations of the calibration and inversion approach described in this paper.

[66] The lidar-derived SWS evolution with fetch observed on 24 March 1998 in the afternoon was validated against in situ and remote sensing measurements made from a buoy and a ship as well as from the spaceborne altimeter TOPEX. The spatial variability in SWS observed with the airborne lidar was controlled by the structure of the wake regions downstream of the Massif Central and the Maritime Alps,

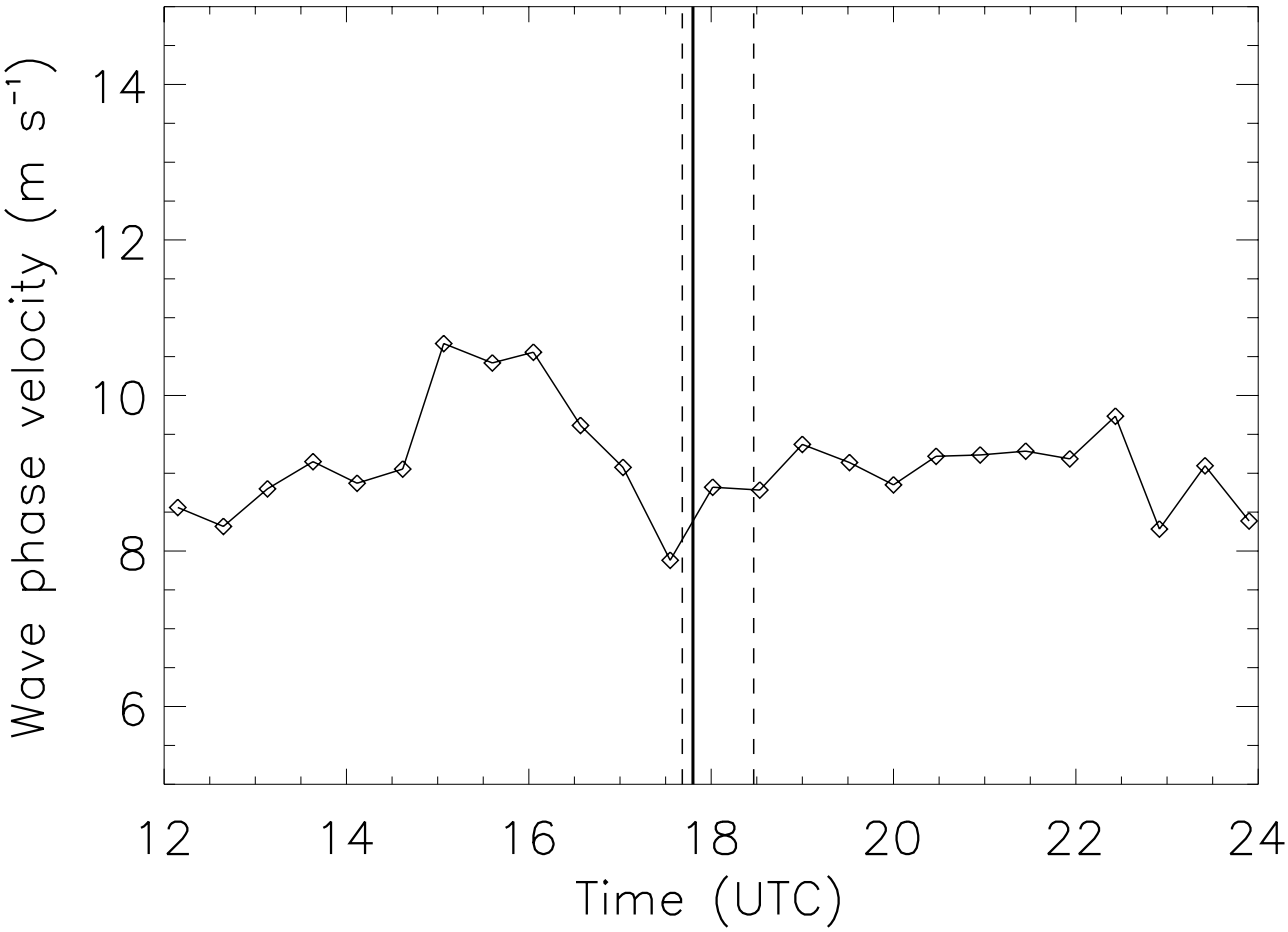

Figure 9. (continued)

delimiting the longitudinal extension of the Mistral, as well as influenced by swell resulting from the action of a steady northeasterly flow coming from the Ligurian Sea in connection with intense Alpine lee cyclogenesis. These findings were supported by the other measurements.

[67] Using a formulation of the dimensionless roughness dependance with inverse wave age given by *Drennan et al.* [2003] (adapted to this case study), we then show that airborne lidar and radar measurements can be combined to provide insight into the evolution with fetch of roughness length, neutral drag coefficient and friction velocity. The remotely sensed variables used as input are the significant wave height and the wave phase velocity (radar) as well as SWS (lidar). Given the sensitivity of the surface roughness determined from the Drennan et al. relationship and the uncertainties associated with above mentioned lidar and radar variables, we felt it was elusive to attempt to determine the "absolute values" of roughness length, neutral drag coefficient and friction velocity from airborne measurements alone. Rather, we have used ASIS measurements to constrain the lidar/radar retrievals at the location of the buoy and focused on the analysis of the evolution of roughness length, neutral drag coefficient and friction velocity with fetch.

[68] Four distinct sea state regimes over a distance of 100 km could be identified from the remotely sensed variables obtained with this novel approach, in connection with atmospheric forcing (namely, the wake region downstream of the Massif Central, the established Mistral, the Mistral flow perturbed by the wake downstream of the Maritime Alps, the northeasterly flow from the Ligurian Sea). The dependance of lidar/radar derived drag coefficient with lidar-derived SWS for the 4 regimes was found to be remarkably consistent with the relationship derived from the buoy measurements. Finally, lidar/radar derived friction velocities were found in good agreement with the buoy and in situ aircraft measurements.

[69] Over the open ocean (neutral stability conditions) in moderate wind conditions (less than 10 m s^{-1}), *Menzies et al.* [1998] were able to retrieve SWSs, with a good accuracy and without a need for exogenous data (submarine reflectance, whitecap coverage, atmospheric stability conditions), using lidar measurements made in the framework of the Lidar In-space Technology Experiment which took place in September 1994. Lidar observations made at the global scale in the framework of future spaceborne missions such GLAS (Geoscience Laser Altimeter System) and CALIPSO (Cloud Aerosol Lidar and Infrared Pathfinder Satellite Observation) could be used to improve the analysis of turbulent heat fluxes in coastal regions when combined with radar and in situ data. The perspective of deriving SWS from lidar measurements in coastal regions where

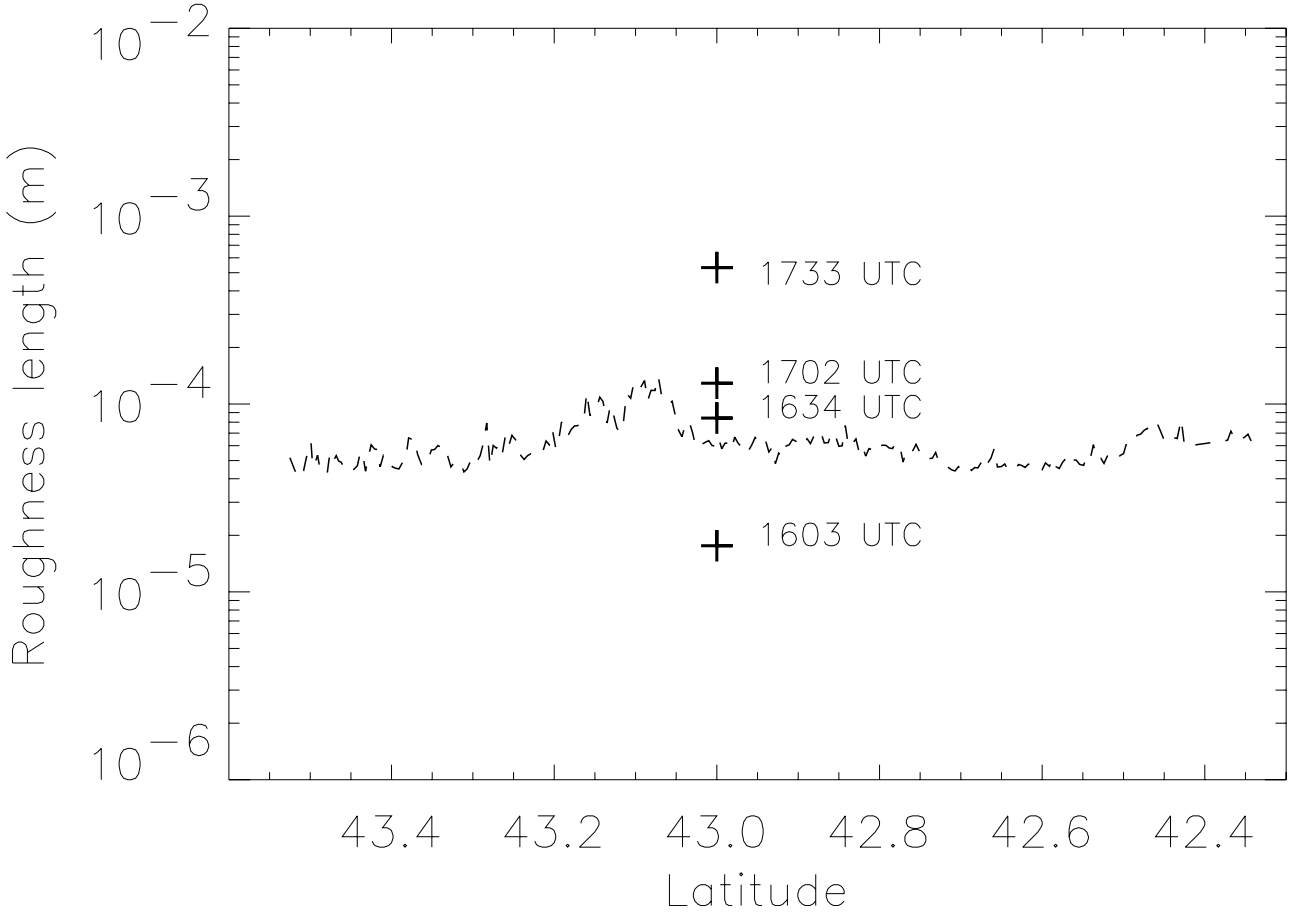

Figure 10. Roughness length evolution with fetch along leg AF. Crosses represent the roughness length estimated from ASIS measurements between 1603 and 1733 UTC.

spaceborne radar retrievals of SWS are known not to be reliable, is extremely appealing.

Appendix A: Solar Radiation and Lidar Background Correction Procedure

[70] In coastal waters, submarine reflectance can be enhanced due to the presence of Chlorophyll, inorganic suspended particles from terrestrial origin, yellow substances (in the Rhone river plume) or even mineral dust (deposited at the surface during Saharan dust outbreaks). As a result, submarine reflectance at selected wavelength can exhibit an important spatial variability at the scale of the GoL. Figure 13 shows the normalized water-leaving radiance, *nLw*, at 670 nm observed by the Sea-viewing Wide Field-of-view Sensor (SeaWIFS) pass over the GoL at 1138 UTC on 24 March 1998 (obtained from the SeaDAS software). The normalized water leaving radiance is approximately the radiance which would exit the ocean in the absence of the atmosphere and with the Sun at zenith. The normalized water-leaving radiance is linked to the subsurface water reflectance ρ_{ssw} by $\rho_{ssw} = \pi nLw/F_o$, where F_o is the solar irradiance at the top of the atmosphere. In Figure 14, we show the correlation existing between the lidar system detected background light (at 732 nm) scattered in the direction of the telescope and the SeaWIFS normalized water-leaving radiance at 670 nm extracted from Figure 13 along leg AF. The background light is the ambient atmospheric light scattered in the direction of the telescope acquired prior to firing the laser, which is in turn subtracted from the subsequent lidar return signals. [A background light measurement is performed prior to the acquisition of each lidar signal profile.] A correlation coefficient of 0.71 (explaining 85% of the observed variance) is obtained. A large part of the variance not explained by the correlation is likely to be related to solar-induced Chlorophyll fluorescence at 670 nm. Finally, some of the scatter observed in Figure 14 can also be explained by the fact that SeaWIFS and lidar measurements were not acquired at the same time. Given the high correlation coefficient, we are confident that solar radiation diffused by the suspended particulates and/or foam in the direction of the lidar telescope is indeed removed through "background" light corrections applied to the lidar data, even though the data presented here only partly supports those conclusions (due to the fact that observations were not made at the same time and wavelength).

Appendix B: Lidar Inversion and Lidar-Derived Sea Surface Reflectance

[71] Sea surface reflectance is inferred from lidar measurements using the method described by *Flamant et al.* [1998], as

$$\widehat{\rho} = \pi \Delta z \beta(\lambda, \pi, z_b) \frac{S(\lambda, z_0)}{S(\lambda, z_b)}. \quad \text{(B1)}$$

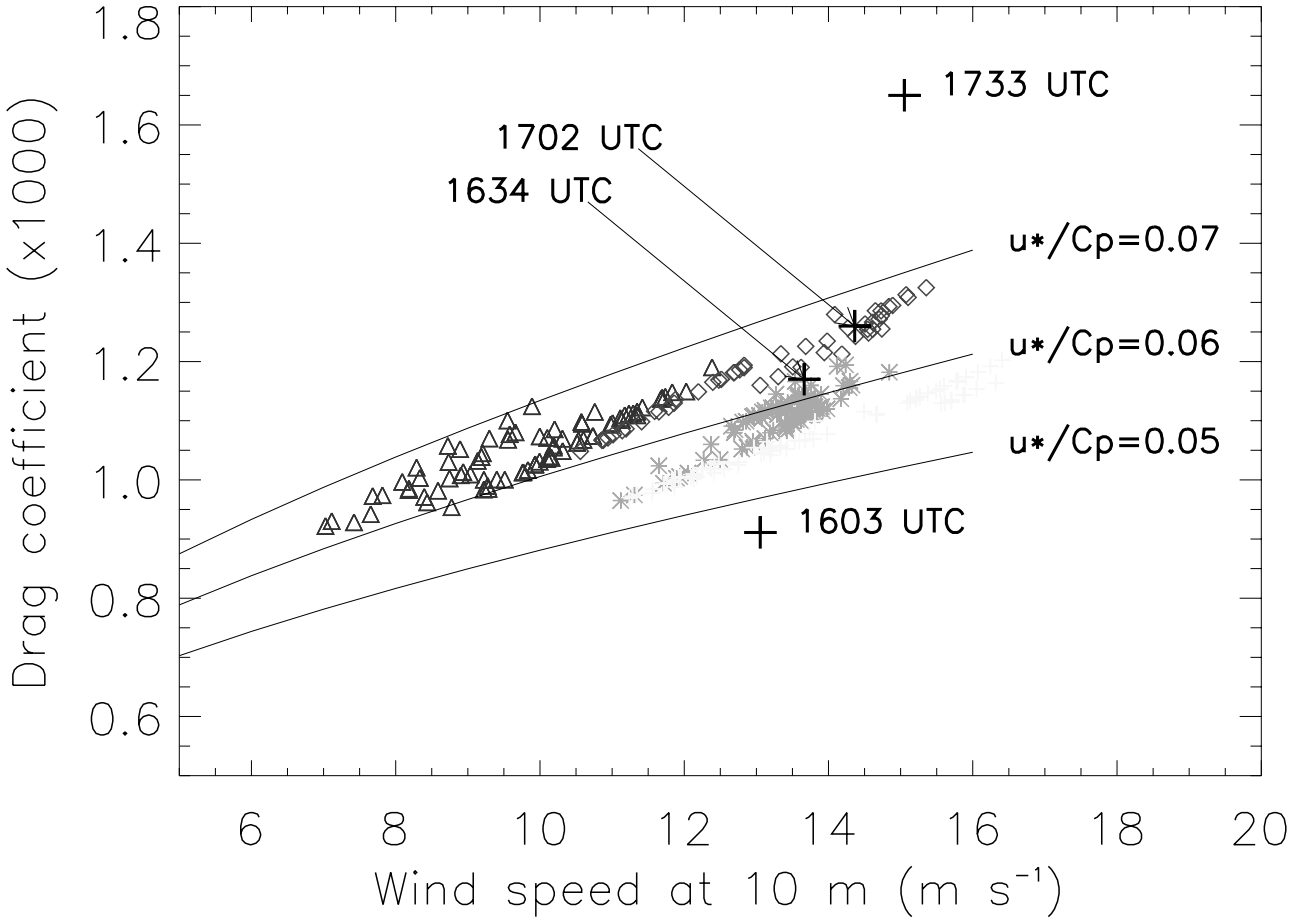

Figure 11. Drag coefficient versus wind speed, both 10 m ASL neutral, for leg AF data. The solid lines are the inverse wave age dependent drag versus wind speed relationships resulting from equations (16), (17) and (18). Drag coefficients are grouped in 4 latitudinal ensembles: between the coast and 43.25°N (blue triangles), between 43.25°N and 43°N (red diamonds), between 43°N and 42.7°N (orange asterisks) and beyond 42.7°N (yellow crosses). Crosses represent the drag coefficients estimated from ASIS measurements between 1603 and 1733 UTC. Note that the inverse wave age corresponding to these points are 0.0468, 0.0545, 0.0616 and 0.0754.

which accounts for the lidar signal $S(\lambda, z_b)$ in the layer close to the surface, the lidar surface return signal $S(\lambda, z_0)$ as well as the average backscatter coefficient $\beta(\lambda, \pi, z_b)$ measured in a layer of depth Δz, at an altitude $z_b = z_0 + \Delta z$ above the surface.

[72] The largest uncertainty on lidar-derived SSR is due to the uncertainty on $\beta(\lambda, \pi, z_b)$ which is obtained from the well-known "lidar inversion" procedure [e.g., *Flamant et al.*, 1998]. In this procedure (see below), accurate $\beta(\lambda, \pi, z_b)$, and hence SSR, estimates can only be obtained if the attenuation of the laser beam by aerosol particles is properly corrected for between the aircraft and the sea surface. This implies that the aerosol population in the atmospheric column sampled by lidar is known (this information enables to calculate a particulate backscatter-to-extinction ratio, BER, profile using the Mie theory). Furthermore, the inversion procedure used in this study also relies on an independant measurement of the scattering ratio (defined as the ratio of the total backscatter coefficient to the molecular backscatter coefficient) at some height in the region of the atmosphere sampled by the laser beam.

[73] During FETCH, the reference scattering ratio necessary to initialize the inversion procedure was measured in situ by a nephelometer on-board the ARAT. To compute the BER, an idealized coastal aerosol population has been defined, based on previous studies undertaken in this region and ship-borne measurements. To compensate, in part, the lack of aerosol measurements, the sensitivity of SSR to the BER and to the reference scattering ratio has been analyzed.

B.1. Reference Scattering Ratio

[74] The reference scattering ratio is obtained from in situ scattering coefficient measurements made at 3.9 km ASL by a Meteorology Research, Inc. (MRI) integrating nephelometer model 1550B mounted on the ARAT. It measures the scattering by both gases and aerosols around 550 nm. No correction for the molecular contribution is applied in real time. The design of the instrument implies that only scattering by extinction, and not scattering by absorption, is measured [*Heintzenberg and Charlson*, 1996]. The sampled air used in this instrument was heated to maintain a relative humidity below 60%. The sampling error on the

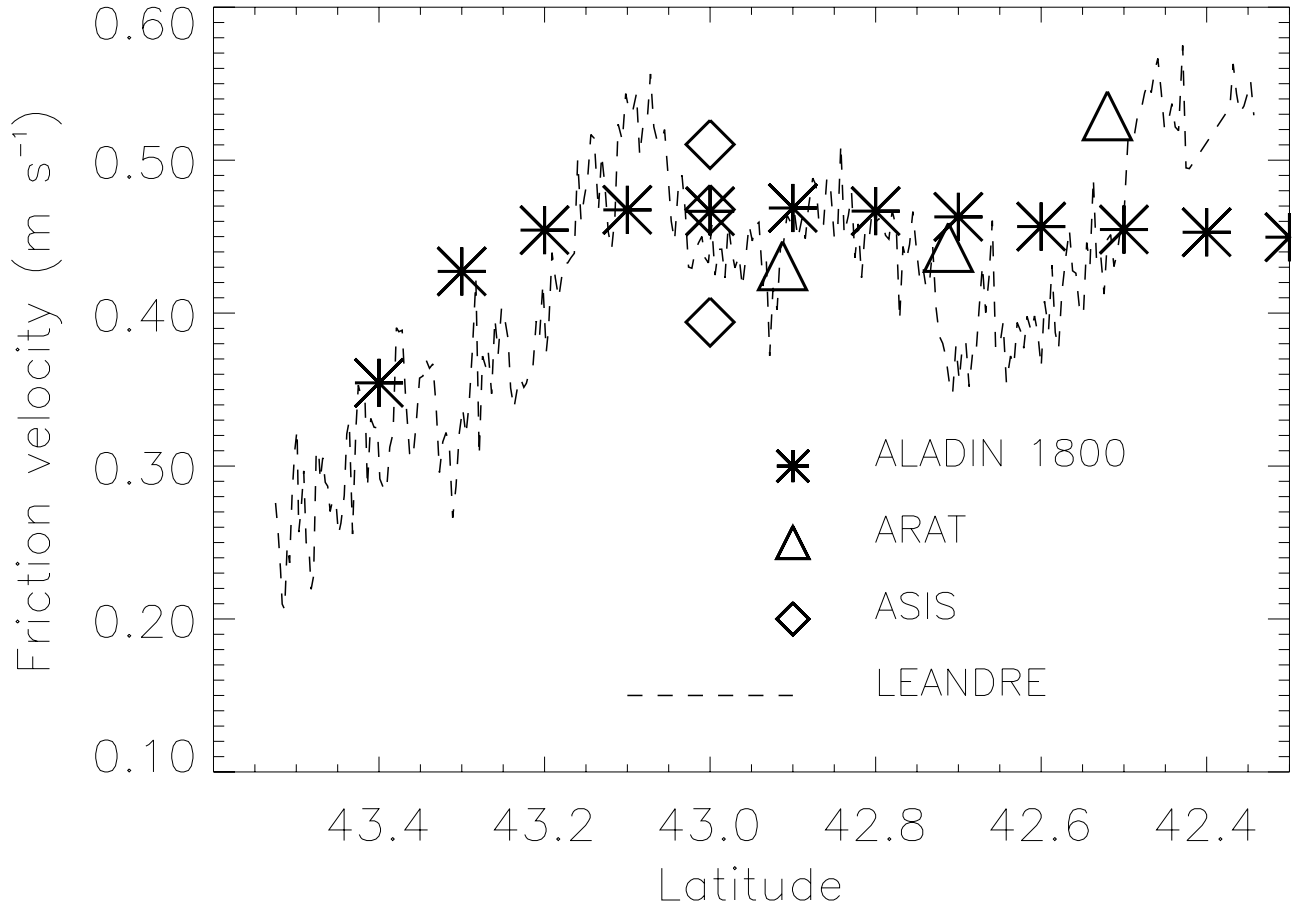

Figure 12. Friction velocity evolution with fetch along leg AF.

measured scattering coefficient is estimated to be of the order of 10% as specified by MRI.

[75] The average value of the scattering ratio at 3.9 km ASL was about 2 (not shown). The statistical variability associated with these measurements was observed to be on the order of 5%, peak to peak. The largest resulting quadratic error (computed as the square root of the errors squared) accounting for measurement uncertainties and statistical variability is 12%. Hence, the reference scattering ratio at 3.9 km ASL was equal to 2.0 ± 0.1 for the entire flight.

B.2. Aerosol Composition and Vertical Distribution

[76] During a Mistral event, the coastal marine aerosol is a dynamic reservoir of particles originating from diverse marine and continental sources. Sea-salt, dust, water-soluble, particulate organic matter and soot can be important contributors to the coastal marine aerosol composition.

[77] During the FETCH experiment, the aerosol composition was analyzed from samples made with a 13-stage low cascade impactor installed on the front deck of the Research Vessel Atalante [*Sellegri et al.*, 2001]. Special attention was paid to water-soluble and sea-salt aerosols. Total carbon and soot concentrations were not measured during FETCH. Size distributions, between 0.5 and 15 μm aerodynamic diameter, were obtained from an active scattering spectrometer probe mounted on the mast located on the front deck of the ship.

[78] On 24 March 1998, 3 aerosol composition samples were collected at 75, 44 and 38 km from the coast. They revealed that an important fraction of the aerosol sampled at the ship was of anthropogenic origin. The bulk concentrations indicated that the sample closest to the coast was characterized by higher anthropogenic compound concentrations and lower sea-salt concentrations than the sample farthest from the coast. The total aerosol concentration derived from these distributions decreased with increasing fetch within 40–50 km from the coast, and increased with fetch beyond. The decrease is most likely related to turbulent deposition of anthropogenic aerosols. Beyond 40–50 km, the increase in aerosol concentration is likely to be related to particle generation by the action of wind at the sea surface.

[79] However, these surface measurements are likely not to be representative of the aerosol composition above the MABL surface layer. On 24 March 1998, the air masses had traveled over the continent prior to being sampled by the aerosol instrumentation on the Atalante. Over warm land, the continental ABL was observed to be about 2 km deep [*Flamant*, 2003]. Due to convection and turbulence, aerosols are generally observed to be well mixed in the vertical, over the depth of the continental ABL, forming a so-called pollution plume. When continental aerosol plumes are advected across the coastline they are forced to rise above the MABL [e.g., *Flamant*, 2003]. As a consequence, a considerable part of the continental ABL particles may be transported over thousands of kilometers without removal by washout processes. Numerous measurements have shown this over the coastal Atlantic Ocean for example [*Flamant et al.*, 2000; *Ansmann et al.*, 2001]. Hence,

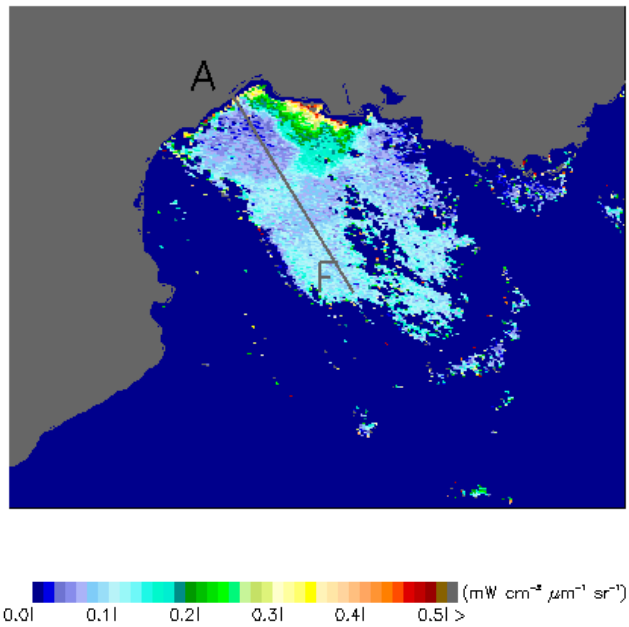

Figure 13. Normalized water-leaving radiance at 670 nm over the GoL observed by the Sea-viewing Wide Field-of-view Sensor (SeaWIFS) pass over the GoL at 1138 UTC on 24 March 1998 (obtained from the SeaDAS software).

(partial) knowledge of the aerosol composition near the surface is not enough for our purpose. However, no measurements of the aerosol composition were made above the sea surface (i.e., from airborne platforms). Therefore, we have assumed the aerosol population over the GoL to be a mixture of the maritime and continental aerosol described by *Ackerman* [1998]. The errors and uncertainties on SSR retrievals associated with this assumption are assessed through sensitivity analyses as detailed in the following.

B.3. Sensitivity, Errors, and Uncertainties on SSR Retrievals

[80] Given the lack of aerosol distribution measurements above the MABL surface layer, we have considered the likely range of variation of the BER in a coastal region based on the work of *Ackerman* [1998]. *Ackerman* [1998] computed the BER fluctuations with relative humidity (RH) for two aerosol (marine and a continental) models and at two wavelengths, i.e., 532 and 1064 nm. Aircraft measurements and ALADIN forecasts were used to determine the range of RH conditions encountered during the flight. RH ranged between 40 and 100% in the MABL, and between 15 and 40% ± 5% aloft. Considering Ackerman's marine aerosol model, we find BER values in the MABL ranging between 0.033 and 0.04 sr^{-1} at 532 nm; and ranging between 0.02 and 0.04 sr^{-1} at 1064 nm. Considering Ackerman's con-

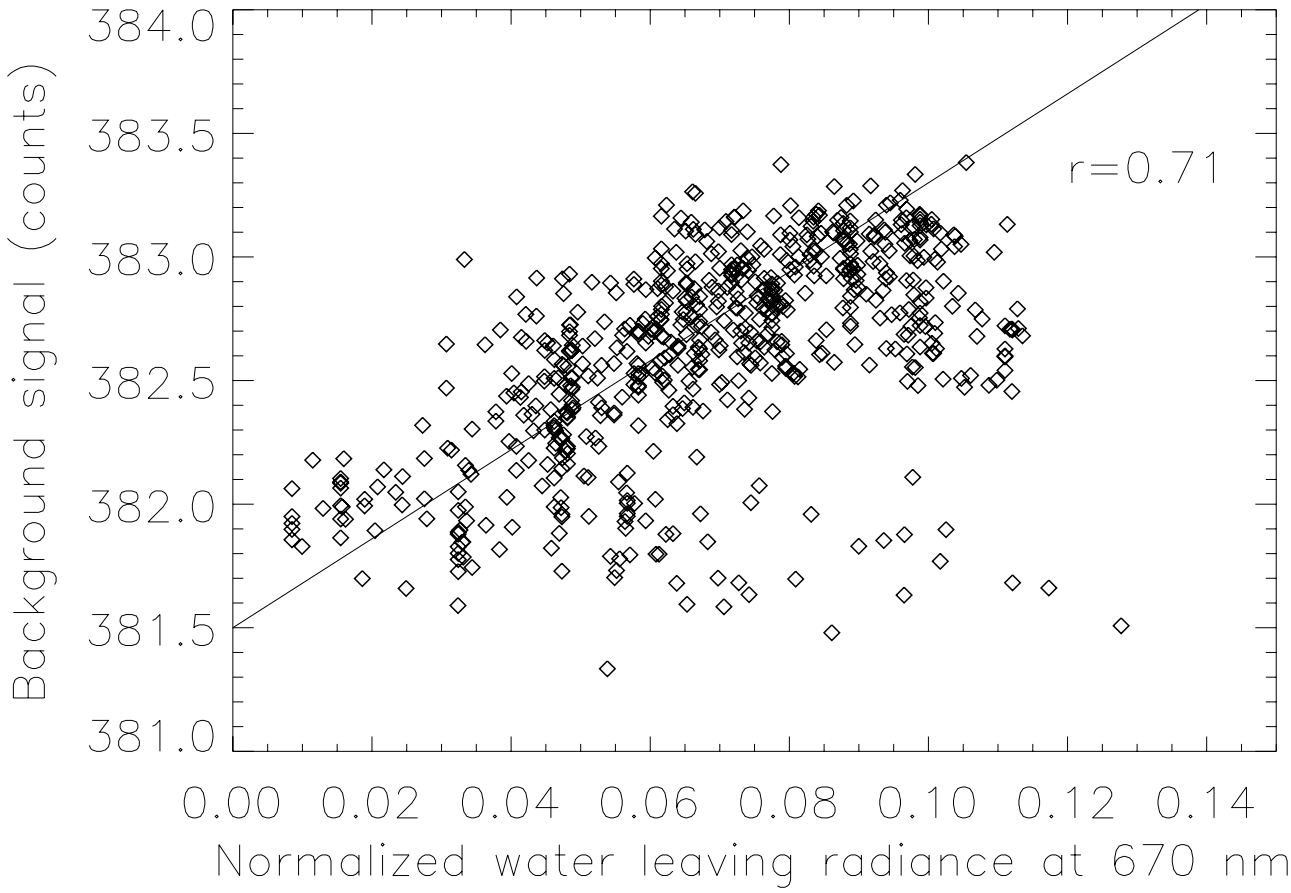

Figure 14. SeaWIFS normalized water leaving radiance at 670 nm versus lidar detected background light at 732 nm.

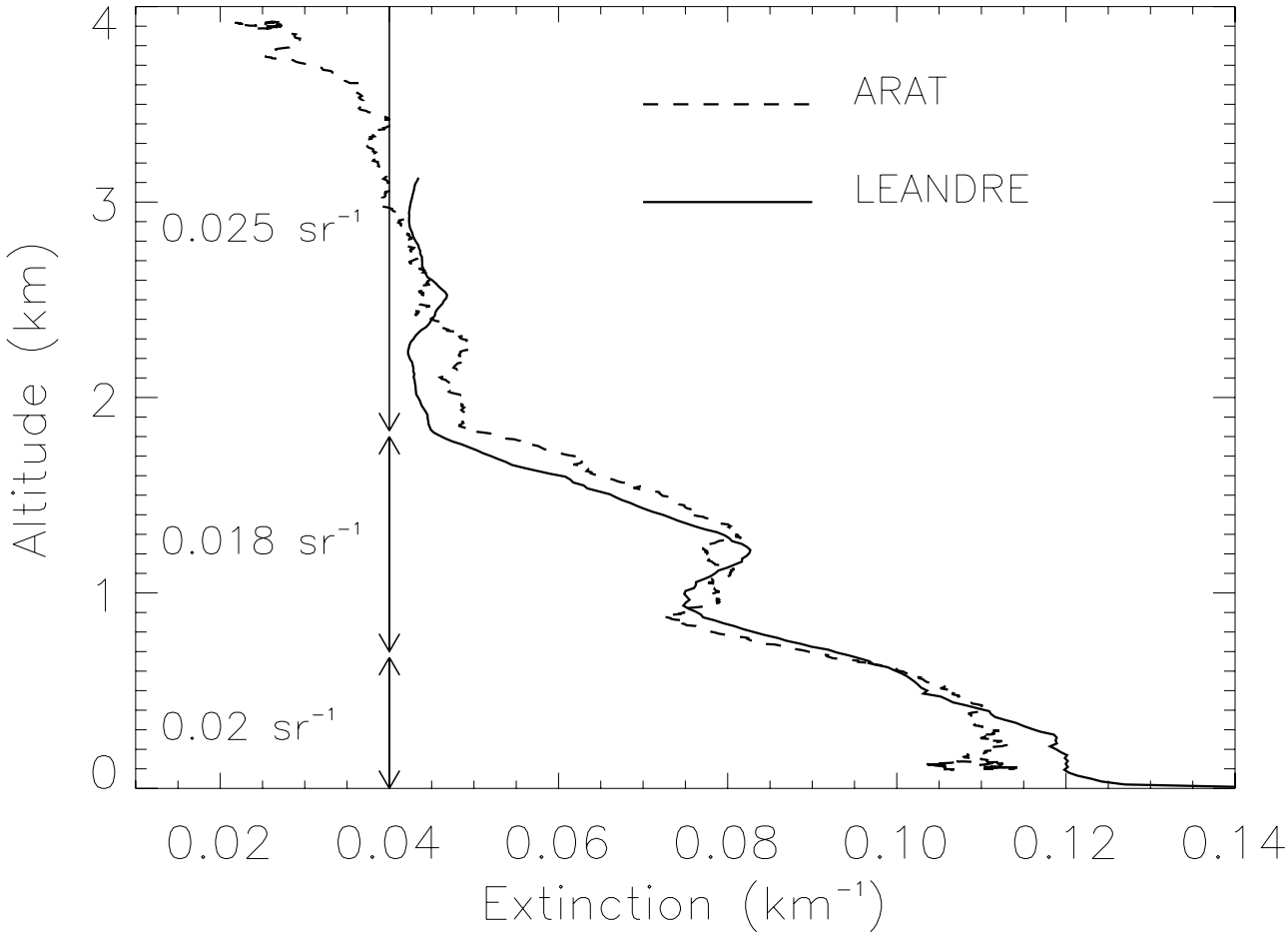

Figure 15. Comparison between the lidar-derived (solid line) and in situ nephelometer (dashed line) total extinction coefficient profile at 550 nm. Also indicated are the BER values (0.02, 0.018 and 0.025 sr^{-1}) used to derived the particle extinction coefficient from lidar data.

tinental aerosol model, we find BER values between 0.022 and 0.024 sr^{-1} at 532 nm; and between 0.018 and 0.022 sr^{-1} at 1064 nm in the advected continental ABL. Hence, the likely range of variation for the BER at 732 nm was considered to be [0.02, 0.04] and [0.018, 0.024], in the MABL and in the continental ABL, respectively.

[81] Over the GoL, the atmosphere was observed to be composed of three layers essentially: an internal thermal MABL developing offshore within the advected continental ABL, and the free troposphere aloft [*Flamant et al.*, 2003]. In the following, we have used the extinction coefficient profile obtained at 550 nm from the in situ nephelometer during a sounding over the GoL (section 2) to constrain the lidar inversion and infer BER values characteristic of each layer. This profile (Figure 15) was acquired in a region where the MABL was approximately 0.7 km deep and the continental ABL approximately 1 km deep (top at 1.7 km ASL). A series of 100 lidar shots acquired in the vicinity of the aircraft sounding (the aircraft sounding was performed at a later time) were used for the lidar inversion.

[82] In order to carry out a meaningful comparison of lidar and nephelometer extinction profiles, lidar extinction profiles were retrieved at 732 nm and transposed to a wavelength of 550 nm assuming a range independent value of the ngstrm coefficient. We then iterated on the BER values in the different layers and on the ngstrm coefficient values until the lidar extinction profile converges within 10% (on average) of the nephelometer extinction profile.

[83] The best agreement between the lidar-derived and nephelometer-derived extinction profiles was found for values of 0.02, 0.018 and 0.025 sr^{-1} in the MABL, continental ABL and free troposphere, respectively, and an ngstrm coefficient of 2.5 (Figure 15). Note that this combination of BER and ngstrm coefficient values is a possible solution of the lidar equation, but by no means is it a unique solution. The BER value of 0.018 sr^{-1} in the continental ABL is in good agreement with the characteristic value for continental aerosol proposed by *Ackerman* [1998]. On the other hand, the BER value derived in the MABL is much less than generally observed in pollution-free conditions, i.e., when the lidar signal is dominated by water solubles, particulate organic matter and sea-salt aerosol. This low value could be an indication of the rather polluted air masses advected over the GoL during the Mistral/tramontane event. Such pollution aerosols were indeed sampled on-board the Research Vessel Atalante [*Sellegri et al.*, 2001].

[84] Finally, the lidar-derived atmospheric reflectivity in the MABL was reported to increase significantly between endpoints A and F [*Flamant*, 2003]. He related the increase

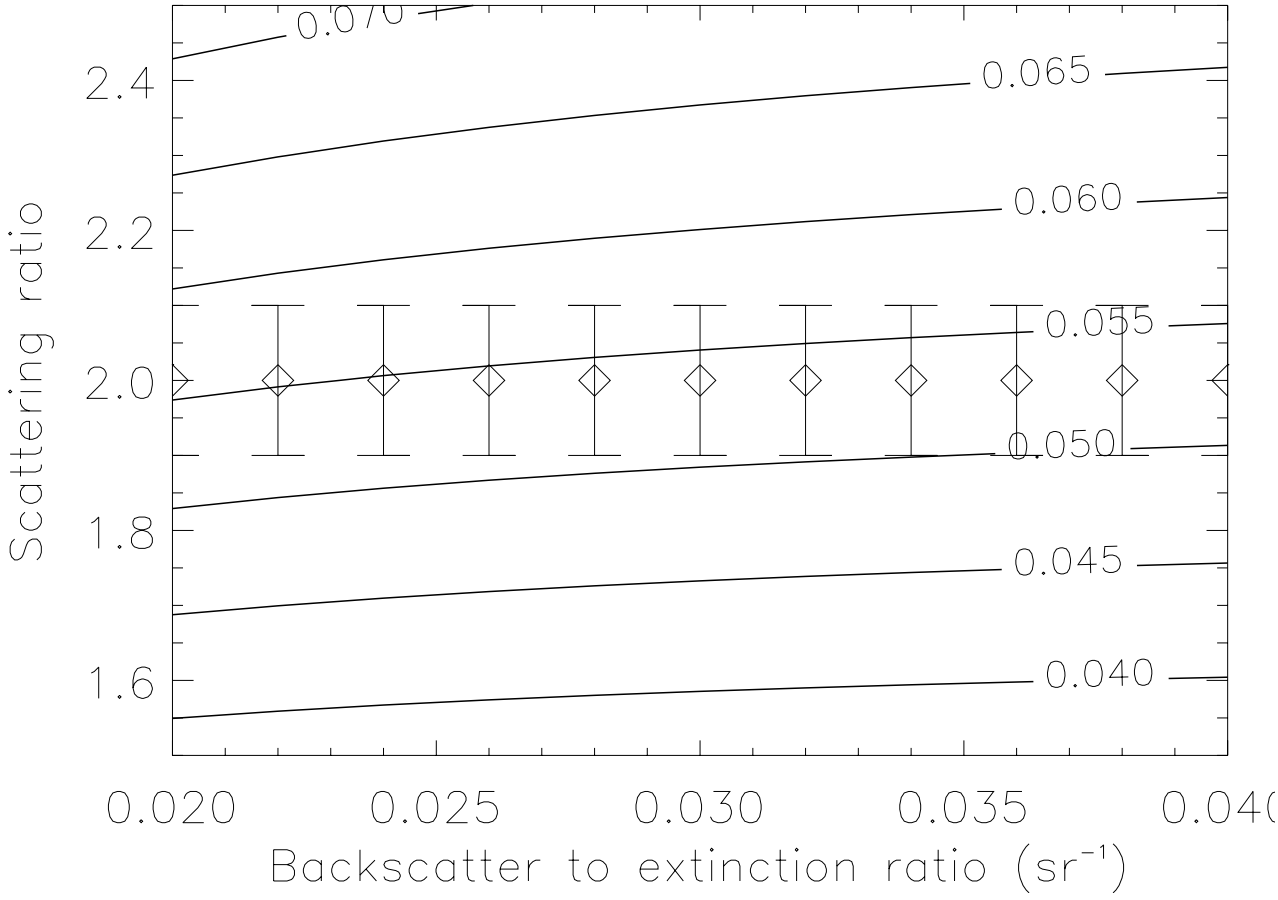

Figure 16. Sensitivity of sea surface reflectance derived from a series of 100 lidar shots over the Gulf of Lion to the BER and to the reference scattering ratio.

of lidar reflectivity observed east of 4.4°E on leg AF to an increase in aerosol concentration and/or a change in aerosol optical properties downwind of the city of Marseille and the industrial petro-chemical complex of Berre/Fos (43.4°N, 4.5–4.6°E, Figure 1). Hence, the BER value obtained near endpoint F may only be representative of the air masses having traveled from the Marseille region. To the west of 4.4°E, air masses could be characterized by commonly assessed BER values of the order of 0.03–0.04 sr^{-1}, rather than the value of 0.02 sr^{-1} near endpoint F. Thus, we have analyzed the sensitivity of SSR (derived from the selected series of 100 lidar shots) to the BER for a 1 km deep MABL in which the BER was varied between 0.02 and 0.04 sr^{-1} (Figure 16). The sensitivity of SSR to the reference scattering ratio is also illustrated in Figure 16. Figure 16 shows that the SSR is very sensitive the reference scattering ratio and only moderately sensitive to the BER. For a scattering ratio equal to 2, the SSR varied between 0.053 and 0.056 for the BER range considered, i.e., about 5%. For a BER of 0.035 sr^{-1}, the SSR varied between 0.05 and 0.057 for a scattering ratio ranging between 1.9 and 2.1, i.e., about 15%. This means that the SWS estimates are not sensitive to the evolution of the composition of the aerosol.

[85] In this study, the lidar data along leg AF have been processed using BER values of 0.02, 0.018 and 0.025 sr^{-1} in the MABL, continental ABL and free troposphere, respectively. The continental ABL top height was taken at 1.8 km ASL and remained unchanged along AF. The structural characteristics of the MABL along leg AF are derived from lidar measurements described by *Flamant* [2003]. These measurements [see *Flamant*, 2003, Figure 14c] showed the internal thermal MABL to reach a depth of 1.2 km at approximately 4.5°E. East of 4.5°E, the MABL structure characteristics over the sea changed dramatically: it was observed to be shallower, with a depth of about 0.7 km. The backscatter coefficient above the sea surface is then derived from each profile along AF and is used to compute the SSR using equation (B1). As mentioned earlier, a constant reference scattering ratio of 2.0 ± 0.1 at 3.9 km ASL was used for the entire leg AF. In the inversion procedure, the ±5% uncertainty on this parameter leads to a 10% uncertainty on the near surface backscatter coefficient [e.g., *Flamant et al.*, 1998].

Appendix C: RESSAC and TOPEX Surface Mean Square Slope Measurements

[86] The radar backscatter cross section (RBCS) per unit area (denoted σ_0, or Normalized Radar Cross Section NRCS) due to specular reflection on a rough surface has been shown by *Barrick* [1968] and *Valenzuela* [1978] to be related to the probability density function (pdf) of ocean surface slope as:

$$\sigma_0 = \rho^2 \pi \frac{1}{\cos^4 \theta} p\left(\zeta'_x, \zeta'_y\right), \qquad \text{(C1)}$$

where θ is the radar incidence angle and ρ^2 is an effective normal incidence reflectivity. The sea surface is defined by the height function $\zeta(x, y)$, ζ'_x, ζ'_y are the slope components in two orthogonal directions, and the slope pdf is denoted $p(\zeta'_x, \zeta'_y)$.

[87] If we assume an isotropic rough surface with Gaussian statistics, equation (C1) becomes:

$$\sigma_0 \cos^4\theta = \frac{\rho^2}{\langle S^2\rangle} \exp\left(-\frac{\tan^2\theta}{\langle S^2\rangle}\right), \tag{C2}$$

where $\langle S^2\rangle$ is the MSS of the slopes pdf.

[88] To estimate the MSS values from the RESSAC data, we analyze the dependence of the NCRS with incidence angle as described by *Hauser et al.* [1992]

$$\left[\sigma_0 \cos^4\theta\right]_s = -4.34\left(-\frac{\tan^2\theta}{\langle S^2\rangle}\right) + \frac{B}{\langle S^2\rangle}, \tag{C3}$$

where $[\sigma_0 \cos^4\theta]_s$ is in dB. The MSS $\langle S^2\rangle$ is obtained from the RESSAC data through a least squares fit of the left-hand side term to $\tan^2\theta$. Because the quasi-specular approximation is valid only for small angles, the range of incidence angles for this least squares fit is limited to [5°, 12°]. This method allows the estimation of the MSS without any knowledge of the Fresnel coefficient, nor of the calibration constant of the radar.

[89] The incidence angle for TOPEX being null (nadir looking), under the Gaussian assumption, the MSS is directly related to the RBCS, and equation (C2) becomes:

$$\sigma_0 = \frac{\rho^2}{\langle S^2\rangle}. \tag{C4}$$

[90] However, the effective reflectivity differs from the Fresnel reflectivity at normal incidence angle due to diffraction from small-scale surface structure. The nominal Fresnel coefficient ρ^2 for seawater is about 0.64 and 0.61, in C-Band and Ku-Band, respectively. For Ku-Band, the effective Fresnel coefficient varies between 0.36 and 0.45 for a wind of 7 to 15 m s^{-1}. The value more often used is about 0.4 [*Jackson et al.*, 1992].

[91] For C-Band, the radar backscatter is not well calibrated, so we chose to adjust the effective coefficient using RESSAC data. First a factor of 0.8 is applied on the RBCS from TOPEX considering the nongaussianity of the slope pdf [see *Chapron et al.*, 2000]. To obtain the same range of MSS values than RESSAC, we adjust the Fresnel coefficient to 0.68. This value is greater than the Fresnel coefficient obtained in C-Band (0.61) by *Elfouhaily et al.* [1998].

[92] **Acknowledgments.** The authors would like to thank their numerous colleagues who have participated to FETCH for acquiring, processing and providing the data, as well as for helpful discussions. Alain Weill is acknowledged for providing the relationship between the fractional area covered by whitecaps and surface wind speed on 24 March 1998. The authors would also like to thank the SeaWiFS Project and the Distributed Active Archive Center at the NASA Goddard Space Flight Center for the production and distribution of the SeaWiFS data acquired at the Dundee station. We are indebted to NASA for providing the SeaDAS software. Marc Mallet and Serge Despiau are acknowledged for fruitful discussions concerning the aerosol measurements made onboard the Research Vessel Atalante. Special thanks to Didier Bruneau, Vincent Trouillet and Pascal Genau of Service d'Aéronomie; Frederic Blouzon, Abdel Abchiche, Nadir Amarouche, Guy Pennazzi, Christian Allet, Noël Grand, André Gribkoff and Bernard Sinardet of the Technical Division (INSU). This research was funded by INSU/CNRS via the PATOM and PNTS programs.

References

Ackerman, J., The extinction-to-backscatter ratio of tropospheric aerosol: A numerical study, *J. Atmos. Oceanic Technol.*, *15*, 1043–1050, 1998.

Ansmann, A., F. Wagner, D. Althausen, D. Müller, A. Herber, and U. Wandinger, European pollution outbreaks during ACE 2: Lofted aerosol plumes observed with Raman lidar at the Portuguese coast, *J. Geophys. Res.*, *106*, 20,725–20,733, 2001.

Banner, M. L., W. Chen, E. J. Walsh, J. B. Jensen, S. Lee, and C. Fandry, The Southern Ocean Waves Experiment, 1, Overview and mean results, *J. Phys. Oceanogr.*, *29*, 2130–2145, 1999.

Barrick, D. E., A relationship between the slope probability density function and the physical optics integral in rough surface scattering, *Proc. IEEE*, *36*, 1728–1729, 1968.

Bidlot, J.-R., 2001: ECMWF wave model products, *ECMWF Newsl.*, *91*, 2001.

Bruneau, D., P. Quaglia, C. Flamant, M. Meissonnier, and J. Pelon, The airborne lidar LEANDRE 2 for water vapor profiling in the troposphere, 1, Description, *Appl. Opt.*, *40*, 3450–3461, 2001a.

Bruneau, D., P. Quaglia, C. Flamant, and J. Pelon, The airborne lidar LEANDRE 2 for water vapor profiling in the troposphere, 2, First results, *Appl. Opt.*, *40*, 3462–3475, 2001b.

Bufton, J. L., F. E. Hoge, and R. N. Swift, Airborne measurements of laser backscatter from the ocean surface, *Appl. Opt.*, *22*, 2603–2618, 1983.

Campins, J., A. Genoves, A. Jansa, J. A. Guijarro, and C. Ramis, A catalogue and a classification of surface cyclones for the Western Mediterranean, *Int. J. Climatol.*, *20*, 969–984, 2000.

Chapron, B., V. Kerboal, D. Vandemark, and T. Elfouhaily, Importance of peakedness in sea surface slope measurements and applications, *Geophys. Res. Lett.*, *105*, 17,195–17,202, 2000.

Chen, W., M. L. Banner, E. J. Walsh, J. B. Jensen, and S. Lee, The Southern Ocean Waves Experiment, 2, Sea surface response to wind speed and wind stress variations, *J. Phys. Oceanogr.*, *31*, 17,195–17,202, 2000.

Cox, C., and W. Munk, Measurements of roughness of the sea surface from photographs of the Sun's glitter, *J. Opt. Soc. Am.*, *44*(11), 832–850, 1954.

Donelan, M. A., Air-sea interaction, in *Ocean Engineering Science*, edited by B. LeMehaute and D. M. Hanes, pp. 239–292, John Wiley, New York, 1990.

Drennan, W., H. C. Graber, D. Hauser, and C. Quentin, On the wave age dependence of wind stress over pure wind seas, *J. Geophys. Res.*, *108*, doi:10.1029/2000JC000715, in press, 2003.

Dupuis, H., J. P. Frangi, and A. Weill, Comparison of wave breaking statistics using underwater noise and sea surface analysis conducted under moderate wind speed conditions during the SOFIA/ASTEX experiment, *Ann. Geophys.*, *11*, 960–969, 1993.

Dyer, A. J., A review of flux-profile relationships, *Boundary Layer Meteorol.*, *7*, 363–372, 1974.

Elfouhaily, T., D. Vandermark, J. Gourrion, and B. Chapron, Estimation of wind stress using dual-frequency TOPEX data, *J. Geophys. Res.*, *103*, 25,101–25,108, 1998.

Eymard, L., A. Weill, D. Bourass, C. Guerin, P. Le Borgne, and J. M. Lefevre, Use of ship mean data for validating model and satellite flux fields during the FETCH experiment, *J. Geophys. Res.*, *108*, doi:10.1029/2001JC001207, in press, 2003.

Flamant, C., Alpine lee cyclogenesis influence on air-sea exchanges and marine atmospheric boundary layer thermodynamics over the western Mediterranean during a Tramontane/Mistral event, *J. Geophys. Res.*, *108*, doi:10.1029/2001JC001040, in press, 2003.

Flamant, C., V. Trouillet, P. Chazette, and J. Pelon, Wind speed dependence of atmospheric boundary layer optical properties and ocean surface reflectance as observed by backscatter lidar, *J. Geophys. Res.*, *103*, 25,137–25,158, 1998.

Flamant, C., et al., Airborne lidar measurements of aerosol spatial distribution and optical properties over the Atlantic Ocean during an European pollution outbreak of ACE-2, *Tellus*, *52B*, 662–677, 2000.

Flamant, C., J. Pelon, L. Eymard, and J. Tournadre, SSM/I integrated water vapor content measurements in coastal regions: A comparison with shipborne and airborne remote sensing measurements, radiosonde measurements, and NWP model retrievals, *J. Geophys. Res.*, *108*, doi:10.1029/2001JC001068, in press, 2003.

Flatau, P. J., M. Flatau, J. R. V. Zaneveld, and C. D. Mobley, Remote sensing of bubble clouds in sea water, *Q. J. R. Meteorol. Soc.*, *126*, 2511–2523, 2000.

Gardner, C. S., B. M. Tsai, and K. E., Multicolor laser altimeter for barometric measurements over the ocean: Theoretical, *Appl. Opt.*, *22*, 2571–2577, 1983.

Gordon, H. R., Diffuse reflectance of the ocean: The theory of its augmentation by chlorophyll fluorescence at 685 nm, *Appl. Opt.*, *18*, 1161–1166, 1979.

Gordon, H. R., and A. Morel, *Remote Assessment of Ocean Color for Interpretation of Satellite Visible Imagery: A Review*, Springer-Verlag, New York, 1983.

Graber, H., E. A. Terray, M. Donelan, W. M. Drennan, J. C. van Leer, and D. B. Peters, ASIS—A new Air-Sea Interaction Spar buoy: Design and performance at sea, *J. Atmos. Oceanic Technol.*, *17*, 708–720, 2000.

Hale, G. M., and M. R. Querry, Optical constants of water in 200-nm to 200-μm wavelength region, *Appl. Opt.*, *12*, 555–563, 1973.

Hasselmann, K., et al., Measurements of wind-wave growth and swell decay during the Joint North Sea Wave Project (JONSWAP), *Dtsch. Hydrogr. Z., Erganz.heft A*, *8* 95 pp., 1973.

Hauser, D., G. Caudal, G. J. Rijckenberg, D. Vidal-Madjar, G. Laurent, and P. Lancelin, RESSAC: A new airborne FM/CW radar ocean wave spectrometer, *IEEE Trans. Geosci. Remote Sens.*, *30*, 981–995, 1992.

Hauser, D., G. Caudal, and L. K. Shay, Behavior of the ocean radar cross-section at low incidence, observed in the vicinity of the gulf stream, *IEEE Trans. Geosci. Remote Sens.*, *33*, 162–171, 1995.

Hauser, D., H. Dupuis, X. Durrieu de Madron, C. Estournel, C. Flamant, J. Pelon, and P. Queffelou, La campagne FETCH: Une expérience pour l'étude des échanges océan/atmosphère dans les conditions côtières du Golfe du Lion, *Météorologie*, *29*, 14–31, 2000.

Hauser, D., et al., The FETCH experiment: An overview, *J. Geophys. Res.*, *108*, doi:10.1029/2001JD001202, in press, 2003.

Heintzenberg, J., and R. J. Charlson, Design and applications of the integrating nephelometer: A review, *J. Atmos. Oceanic Technol.*, *13*, 987–999, 1996.

Hwang, P. A., and O. H. Shemdin, The dependence of sea surface slope on atmospheric stability and swell conditions, *J. Geophys. Res.*, *93*, 13,903–13,912, 1988.

Jackson, F. C., W. T. Walton, and C. Y. Peng, A comparison of in situ and airborne radar observations of ocean wave directionality, *J. Geophys. Res.*, *90*, 1005–1018, 1985.

Jackson, F. C., W. T. Walton, D. E. Hines, B. A. Walter, and C. Y. Peng, Sea surface mean square slope from Ku-Band backscatter data, *J. Geophys. Res.*, *97*, 11,411–11,427, 1992.

Koepke, P., Effective reflectance of oceanic whitecaps, *Appl. Opt.*, *23*, 1816–1824, 1984.

Louis, J.-F., M. Tiedtke, and J.-F. Geleyn, A short history of the operational PBL-parameterization at ECMWF, *ECMWF Workshop Proceedings on "Planetary Boundary Layer Parameterization"*, pp. 59–79, 1981.

Mahrt, L., D. Vickers, J. Howell, J. Hojstrup, J. M. Wilczak, J. Edson, and J. Hare, Sea surface drag coefficients in the Riso Air Sea Experiment, *J. Geophys. Res.*, *101*, 14,327–14,335, 1996.

Menzies, R., D. M. Tratt, and W. H. Hunt, Lidar In-Space Technology Experiment measurements of the sea surface directional reflectance and the link to surface wind speed, *Appl. Opt.*, *37*, 5550–5559, 1998.

Monahan, E. C., The ocean as a source of atmospheric particles, in *The Role of Air-Sea Exchange in Geochemical Cycling*, edited by P. Buat Menard, pp. 129–163, D. Reidel, Norwell, Mass., 1986.

Pettersson, H., H. C. Graber, D. Hauser, C. Quentin, K. K. Kahma, W. Drennan, and M. A. Donelan, Directional wave measurements from three wave sensors during the FETCH experiment, *J. Geophys. Res*, *108*, doi:10.1029/2001JC001164, in press, 2003.

Sellegri, K., J. Gourdeau, J. P. Putaud, and S. Despiau, Chemical composition of marine aerosol in Mediterranean coastal zone during the FETCH experiment, *J. Geophys. Res.*, *106*, 12,023–12,037, 2001.

Shaw, J. A., and J. H. Churnside, Scanning-laser glint measurements of sea-surface slope statistics, *Appl. Opt.*, *36*, 4202–4213, 2001.

Trigo, I. F., T. D. Davies, and G. R. Bigg, Objective climatology of cyclones in the Mediterranean region, *J. Clim.*, *12*, 1685–1696, 1999.

Valenzuela, G. R., Theories for the interaction of electromagnetic and oceanic waves—A review, *Boundary Layer Meteorol.*, *13*, 61–85, 1978.

Vickers, D., and L. Mahrt, Fetch limited drag coefficients, *Boundary Layer Meteorol.*, *85*, 53–79, 1997.

Witter, D. L., and D. B. Chelton, A geosat altimeter wind speed algorithm and a method for altimeter wind speed algorithm development, *J. Geophys. Res.*, *96*, 8853–8860, 1991.

B. Chapron, F. Gohin, and J. Gourrion, Département d'Océanographie Spatiale DRO/OS, Ifremer Brest, BP 70, 29280 Plouzané, France. (Betrand.Chapron@ifremer.fr; Francis.Gohin@ifremer.fr; Jerome.Gourrion@ifremer.fr)

W. M. Drennan, Rosenstiel School of Marine and Atmospheric Science, University of Miami, Miami, FL, USA. (wdrennan@rsmas.miami.edu)

C. Flamant and J. Pelon, Service d'Aéronomie, Université Pierre et Marie Curie, Boîte 102, 4 place Jussieu, 75252 Paris, Cedex, France. (cyf@aero.jussieu.fr; jpe@aero.jussieu.fr)

D. Hauser and C. Quentin, Centre d'Étude des Environnements Planétaires, Université St Quentin-Versailles, 10–12 avenue de l'Europe, 78140 Vélizy, France. (Daniele.Hauser@cetp.ipsl.fr; Celine.Quentin@cetp.ipsl.fr)